Quarterly Report for

January 1998 - March 1998

Stanford Geothermal Program

DE-FG07-95ID13370

Table of Contents

1. MEASUREMENTS OF STEAM-WATER RELATIVE PERMEABILITY

This research project is being conducted by Research Assistant Glenn Mahiya and Prof. Roland N. Horne. The aim is to measure experimentally relative permeability relations for steam and water flowing simultaneously in geothermal rocks.

1.1 SUMMARY

In the earlier quarterly reports, we reported two sets of steam-water relative permeability relations obtained from a successful steady-state experiment conducted under non-adiabatic conditions. The saturations in these experiments were measured by using a high resolution X-ray computer tomography (CT) scanner. In addition the pressure gradients were obtained from accurate measurements of liquid-phase pressure over regions with flat saturation profiles. These two aspects constituted a major improvement in the experimental method compared to those used in the past.

The second set of experiments, reported in the last quarterly report, attempted to repeat the previous experiment with further improvements in steam and hot water injection and water supply feeding systems. Two successful relative permeability experiments were conducted for both steam-water and nitrogen-water fluid pairs with the same core holder. The core holder used in this experiment was different than the one which was used in the previous experiment. Unfortunately, the experiment was not a success, as permeabilities to steam reached unrealistic values. This may have been caused by removal of fines from the core leading to an actual enhancement of the (absolute) permeability, or to experimental errors not yet determined.

Last quarter's disappointing results led us to rethink the design of the experiment, and a new experimental approach will be used. The new procedure and coreholder design will be discussed here.

1.2 EXPERIMENTAL DESIGN

Although the X-ray CT scanner allows us to measure in-situ (static) water and steam saturations with good accuracy, one of the remaining difficulties with the experiment is the problem of determining the *flowing* saturations. To determine the relative permeability, it is necessary to know the individual flow rates of steam and water, and the obvious difficulty is that phase change causes the steam and water rates to vary as a function of position and time. In the current experimental design, the water and steam saturations are determined by careful accounting of the heat losses along the core, so that the enthalpy of the flowing fluid can be estimated based on knowledge of the flow rates and enthalpies of the two injection streams. This approach was adopted because of our desire to avoid the shielding and shadowing of the X-rays if a metallic heater were present on the outside of the core. However, we have recently identified a type of thin-film heating element that offers minimal attenuation to the X-rays, and which therefore holds promise as a guard heater for our experiment. We have tested small sections of this

type of heater and determined: (a) the heater allows us to control the heat loss from the core without difficulty, and (b) the heater is transparent to X-rays in our CT scanner. Using the guard heater with a heat flux sensor placed between it and the core, we have been able to adjust the power to the heater to set the heat flux to zero. This means that the enthalpy of the injected fluid will be maintained along the entire length of the core, and the determination of the flowing steam and water saturations will be much simpler. This will greatly improve the accuracy of the relative permeability measurement.

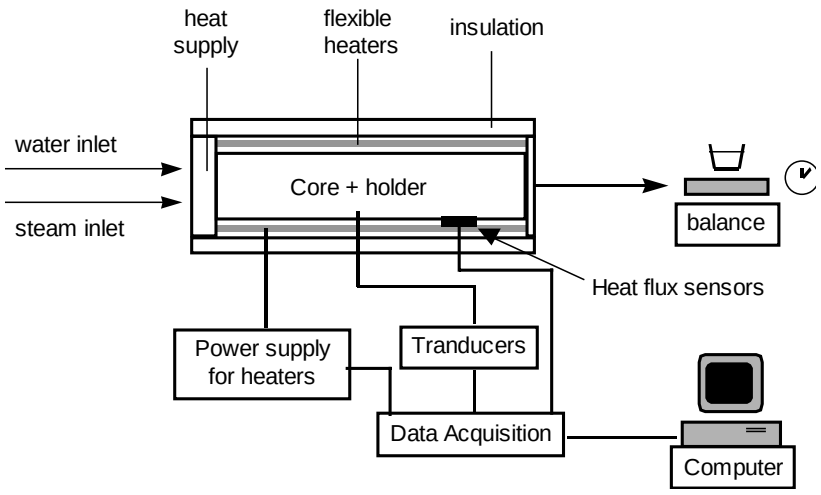

Figure 1.1: Experimental setup for the flow-through experiment using heat guards

It should be noted that the new approach leads to an adiabatic experiment, whereas our approach so far has been to use non-adiabatic experiments.

1.3 PLANS

In the coming quarter we will obtain an 18-segment thin-film heater, and install it on our existing core holder as shown in Figure 1.1. This heater will be fabricated to our design, and has a heat output based on our preliminary testing of single strips and on the measured heat fluxes from earlier experiments. Each segment of the heater will be one inch in length and will cover the entire circumference of the core. 18 heat flux sensors will be used to monitor the heat flux from the core over each 1-inch strip, and the power to each heater strip will be controlled using our existing computer data acquisition and control devices, with the addition of a multichannel solid-state relay output board.

2. MODELING MULTIPHASE BOILING FLOW IN POROUS AND FRACTURED MEDIA

This research project is currently being conducted by Research Assistant Glenn Mahiya, Dr. Cengiz Satik and Professor Roland Horne. The aim of this project is to characterize boiling in homogeneous and fractured porous media.

2.1 OVERVIEW

In the previous quarterly report, we described the experimental setup for boiling in a fractured porous medium. The objective of this experiment is to observe how the boiling front progresses in the presence of a fracture of cylindrical symmetry. This was supposedly an extension of Dr. Cengiz Satik's experiments in 1997 which investigated boiling in a homogeneous core. Relative permeability curves for flow in the fracture were to be inferred from the experiment through numerical simulation using TOUGH2. This was to be achieved by matching measured and simulated pressure, temperature and heat flux profiles, or by estimating thermal properties through inverse calculations provided by ITOUGH2.

In the course of preparations for the experiment, the original Berea sandstone core (used in the homogeneous experiments by Dr. Cengiz Satik in 1997) failed mechanically. This meant having to use a new core on which we intended to conduct another set of homogeneous (non-fractured) experiments followed by fractured experiments in order to make the comparison more appropriate.

The difficulties associated with inferring relative permeabilities from these boiling experiments (see Section 3) have led us to reconsider the technique that we have used so far. The limited extent of the boiling zone in the vertical boiling experiment is one reason why a good match between measured and simulated data has been elusive. We are, therefore, redirecting this research work into a more definitive way of obtaining relative permeability functions. Flow-through experiments will be the focus of our work, as described in Section 1. The main difference between the boiling experiment and the flow-through experiments is that fluid (water and steam) is injected into the core instead of heat being introduced from one end.

3. ESTIMATION OF RELATIVE PERMEABILITY FROM A DYNAMIC BOILING EXPERIMENT

This project was conducted by Research Assistant, Marilou T. Guerrero, Cengiz Satik, and Roland Horne, in collaboration with Stefan Finsterle. The aim of the study was to estimate the relative permeability from a transient vertical boiling experiment. This project was completed in the current quarter, and a technical report was issued on the results.

3.1 INTRODUCTION

Relative permeability is one of the parameters required in describing multiphase flow in porous media since it governs movement of one phase or component with respect to another. It has been studied widely for oil applications (e.g. waterflooding and gas injection), but less so for geothermal applications, which is the main concern of this study. So far, relative permeability relations for steam and liquid water have been based on theoretical methods using field data (e.g. Grant, 1977; Horne and Ramey, 1978), and laboratory experiments (e.g. Ambusso, 1996; Satik, 1998). Although relative permeability is best determined through laboratory experiments, it is difficult to measure due to capillary forces that introduce nonlinear effects on the pressure and saturation distribution at the core exit (Ambusso, 1996). Also, relative permeability is difficult to measure directly for steam-water flows due to experimental constraints (Satik, 1997b). Thus, this study describes a different approach to estimating the relative permeability by matching data from a transient boiling experiment performed on a Berea sandstone to results obtained from numerical simulation. This method provides a way to examine the validity of the relative permeability measurements taken from previous experiments, as well as to estimate capillary pressure.

Although the focus of this research project is relative permeability, capillary pressure has also been studied. These two parameters cannot be separated from each other since they are both important in the behavior of multiphase flow in porous media. However, like relative permeability, capillary pressure in steam-water systems is unknown. This makes the estimation process more difficult because the higher number of unknowns in the problem. In addition, other unknown parameters, such as heat input and heat losses, affect the successful estimation of the relative permeability. To decrease the correlation between the thermal properties and two-phase parameters of interest, the inversion was performed in two steps. Several relative permeability and capillary pressure models were used to solve the inverse problem. The function that best matches the observed data without over-parameterization can be considered the likely scenario.

This report will briefly summarize a few common relative permeability and capillary pressure models. Then a description of the experimental apparatus and procedures will be given, followed by a discussion of the steps involved in the numerical simulation. This report will end with an analysis of results and conclusion of the study.

3.2 RELATIVE PERMEABILITY AND CAPILLARY PRESSURE MODELS

Several semi-empirical relative permeability and capillary pressure relationships have been proposed by different authors. However, only four relative permeability and four capillary pressure models are included in this study. These are the linear, Corey, and Leverett models, and coupled relative permeability and capillary pressure functions, the Brooks-Corey and van Genuchten models. The selection of the models was based on the experimental results obtained by Ambusso (1996) and Satik (1998).

3.2.1 Linear Model

The linear functions comprise the simplest relative permeability (Fig. 3.1) and capillary pressure model. They are given by

k_{rl} increases linearly from 0 to 1 in the range $S_{lr} \le S_l \le S_{ls}$ ……. (3.1)

k_{rg} increases linearly from 0 to 1 in the range $S_{gr} \le S_g \le S_{gs}$ ……..…….. (3.2)

P_{cmax} increases linearly from $S_l = 0$ to $S_l = 1$ ……..…….……. (3.3)

where k_{rl} is the liquid relative permeability, k_{rg} is the gas relative permeability, S_l is the liquid saturation, S_{lr} is the residual liquid saturation or the liquid saturation at $k_{rl}=0$, S_{ls} is the liquid saturation at $k_{rl}=1$, S_{gr} is the residual gas saturation or the gas saturation at $k_{rg}=0$, S_{gs} is the gas saturation at $k_{rg}=1$, and P_{cmax} is the maximum capillary pressure.

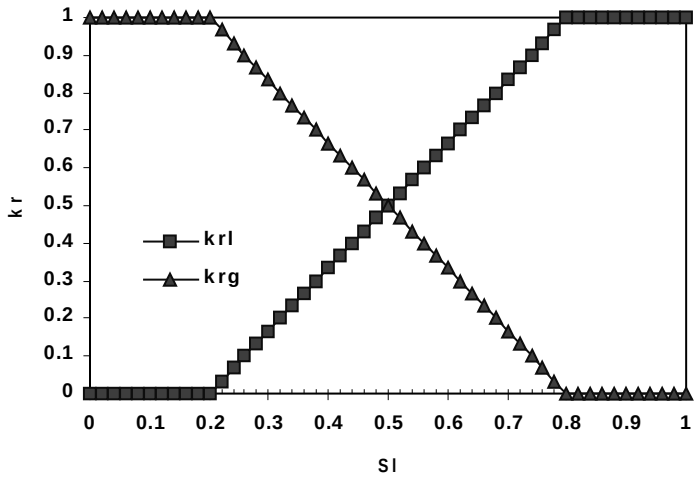

Figure 3.1 Linear relative permeability.

3.2.2 Corey Model

The Corey relative permeability functions (Fig. 3.2), obtained in 1954, are given by

$$k_{rl} = S_e^{\,4} \quad \text{(3.4)}$$

$$k_{rg} = (1 - S_e)^2 (1 - S_e^{\,2}) \quad \text{(3.5)}$$

where

$$S_e = (S_l - S_{lr}) / (1 - S_{lr} - S_{gr}) \quad \text{(3.6)}$$

These relationships were determined from experiments with a variety of porous rocks that had a pore size distribution index of around 2, which is a typical value for soil materials and porous rocks (Corey, 1994).

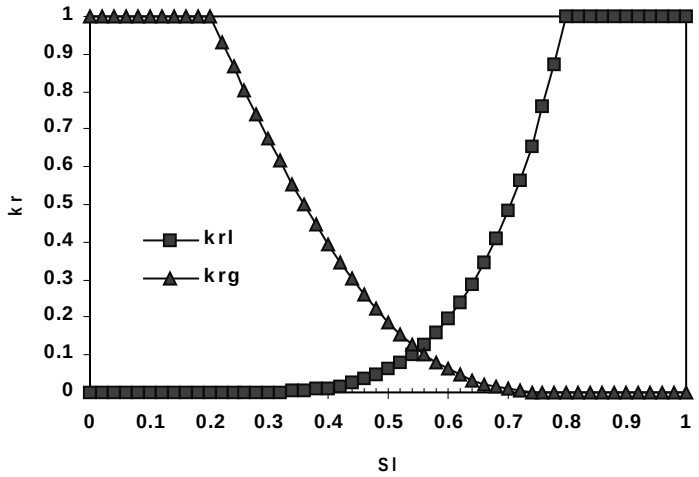

Figure 3.2 Corey relative permeability.

3.2.3 Leverett Model

Leverett (1941) defined a reduced capillary pressure function, which was eventually named Leverett J function by Rose and Bruce (1949) and used for correlating capillary pressure data. Expressing the Leverett J function in terms of capillary pressure

$$p_c = -P_o \, \sigma(T) \, J \quad \text{(3.7)}$$

where

$$J = 1.417\,(1 - S^*) - 2.120\,(1 - S^*)^2 + 1.263\,(1 - S^*)^3 \quad \text{(3.8)}$$

$$S^* = (S_l - S_{lr}) / (1 - S_{lr}) \quad \text{(3.9)}$$

σ is the surface tension of water and P_o is a scale factor. One limitation of the function is that it cannot account for the individual differences between the pore structures of various materials since the scale factor, $P_o = \sqrt{k/\phi}$, is inadequate (Dullien, 1992).

3.2.4 Brooks-Corey Model

The Brooks-Corey functions (Fig. 3.3), obtained in 1964, are given by

$$k_{rl} = S_{ek}^{(2-3\lambda)/\lambda} \quad \text{(3.10)}$$

$$k_{rg} = (1 - S_{ek})^2 (1 - S_{ek}^{(2-3\lambda)/\lambda}) \quad \text{(3.11)}$$

where

$$S_{ek} = (S_l - S_{lr}) / (1 - S_{lr} - S_{gr}) \quad \text{(3.12)}$$

and λ is the pore size distribution index. These relationships are simplifications of the generalized Kozeny-Carman equations and were verified experimentally by Brooks and Corey (1964), and Laliberte et al. (1966). Brooks and Corey found that for typical porous media, λ is 2. Soils with well-developed structures have λ values less than 2, and sands have λ values greater than 2 (Corey, 1994).

The Brooks-Corey capillary pressure function is given by

$$p_c = -p_e \left[\varepsilon / (1 - S_{lr})\right]^{-1/\lambda} - (p_e / \lambda)\left[\varepsilon / (1 - S_{lr})^{(1-\lambda)/\lambda}\right](S_l - S_{lr} - \varepsilon) \quad \text{for } S_l < (S_{wr} + \varepsilon) \quad \text{(3.13)}$$

$$p_c = -p_e (S_{ec})^{-1/\lambda} \quad \text{for } S_l \geq (S_{wr} + \varepsilon) \quad \text{(3.14)}$$

where

$$S_{ec} = (S_l - S_{lr}) / (1 - S_{lr}) \quad \text{(3.15)}$$

and p_e is the gas entry pressure. Equations 3.10 and 3.11 are modified Brooks-Corey equations. To prevent the capillary pressure from increasing to infinity as the effective saturation approaches zero, a linear function is used for $S_l < (S_{lr} + \varepsilon)$, where ε is a small number (Finsterle, 1997). The Brooks-Corey capillary pressure function has been modified for numerical simulation purposes.

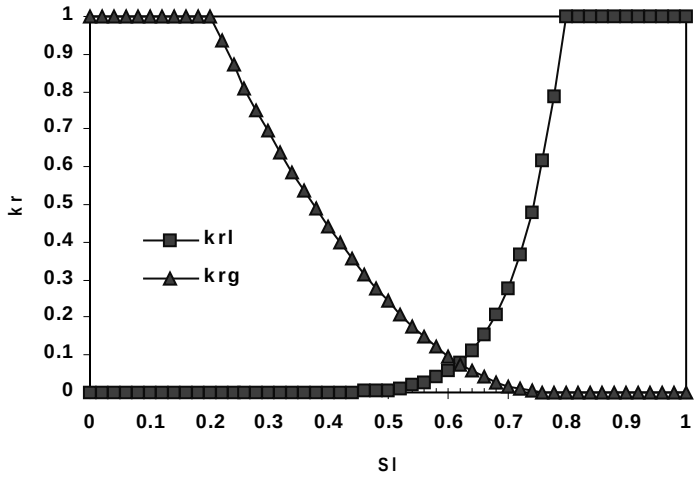

Figure 3.3 Brooks-Corey relative permeability.

3.2.5 van Genuchten Model

The van Genuchten relative permeability (Fig. 3.4) and capillary pressure functions are given by

$$k_{rl} = S_{ek}^{1/2}\left[(1-(1-S_{ek}^{1/m})^{m}\right]^{2} \quad \text{..... (3.16)}$$

$$k_{rg} = (1-S_{ek})^{1/3}\left[1-S_{ek}^{1/m}\right]^{2m} \quad \text{..... (3.17)}$$

$$p_c = -\frac{1}{\alpha}\left[(S_{ec})^{-1/m}-1\right]^{1/n} \qquad \text{for } S_l \geq (S_{wr}+\varepsilon) \quad \text{(3.18)}$$

p_c = linear model with continuos slope at $S_l = S_{wr}+\varepsilon$ for $S_l < (S_{wr}+\varepsilon)$ (3.19)

where

$m = 1 - 1/n$ ..... (3.20)

The parameter, n is analogous to λ, and α is analogous to p_e in the Brooks-Corey functions. Equations 3.15 and 3.16 are modified versions of the van Genuchten equations. In order to prevent the capillary pressure from going to infinity as the liquid saturation approaches zero, a linear function is used for $S_l<(S_{lr}+\varepsilon)$, where ε is a small number (Finsterle, 1997).

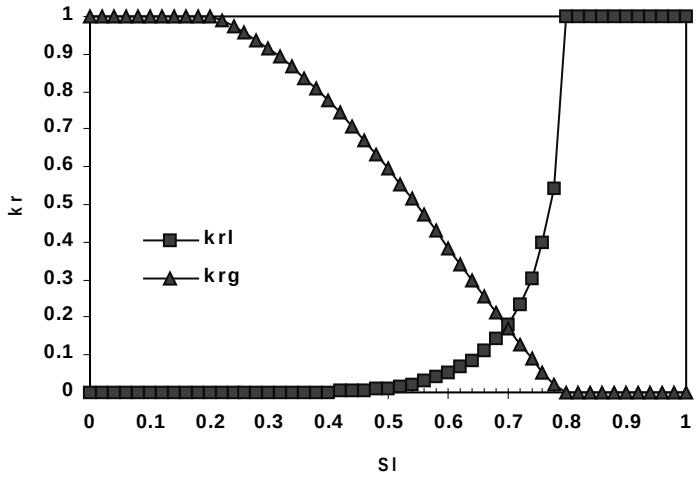

Figure 3.4 van Genuchten relative permeability.

3.3 EXPERIMENTAL APPARATUS AND PROCEDURE

The vertical boiling experiment considered in this study was conducted by Satik (1997a). Figure 3.5 shows a schematic diagram of the apparatus, which consists of a core holder, a data acquisition system, and a balance. A Berea sandstone core was used in the experiment. The core had a diameter of 5.08 cm, length of 43.2 cm, absolute permeability of 780 md, and average porosity of 22% (Table 3.1). Before conducting the experiment, the core was evacuated and then saturated with pre-boiled water to ensure that there was no air trapped in the pore space. The core was confined in an epoxy core holder to prevent fluid from leaking and insulated with a 5.08-cm thick fiber blanket to minimize heat losses in the radial direction. The heater was attached to the bottom of the core, and was

insulated with ceramic fiberboard. During the experiment, the heating end of the core was closed to fluid flow while the opposite end was connected to a water reservoir placed on a balance. The balance was used to monitor the amount of water coming out of the core during the boiling process (Fig. 4.1).

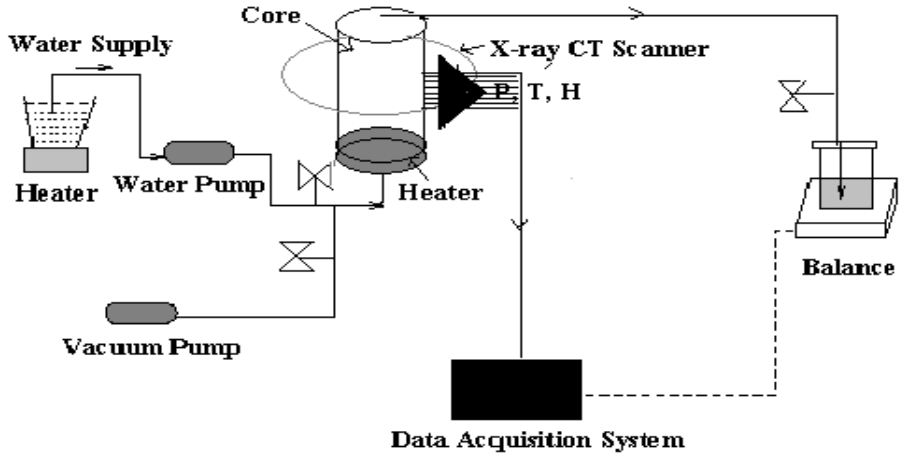

Figure 3.5 Schematic diagram of the experimental apparatus (after Satik, 1997b).

During the experiment, pressure was measured in the core using pressure transducers at 11 locations along the core. Temperature was measured between the epoxy and core insulation using thermocouples that were located at the same points as the pressure transducers. In previous experiments, Satik (1997b) found out that the maximum difference between the temperature in the center of the core and the wall temperature was less than 2^{o}C. This suggested that the radial temperature gradient along the core was not significant under these experimental conditions and therefore it would be adequate to measure wall temperatures only. Similarly, heat flux was measured between the epoxy and core insulation and at the inlet end of the core holder. Steam saturation was measured at every 1-cm increment along the core using a CT scanner. The heat flow rate was increased every time steady-state flow conditions had been reached. At each heat flow rate increase, steady state conditions were observed when the water production rate became zero, and the pressure, temperature, and heat flux measurements stabilized during boiling. Results showed that boiling occurred 118 hours after the start of the experiment that lasted for 169.5 hours. In the plots shown, T1, P1, Sst1, and H1 are temperature, pressure, steam saturation, and heat flux data measured at sensor 1 (1 cm from the heater), T2, P2, Sst2, and H2 are data observed at sensor 2 (5 cm from the heater), etc.

Table 3.1. Physical properties of the cores, epoxy, core insulation, and heater insulation.

Material	ϕ	K	α	C	ρ
	%	10^{-15} m^2	W/m-^{o}C	J/kg-^{o}C	kg/m^3
Berea	22	780	4.326	858.2	2163
Epoxy			2.885	1046.6	1200
Core insulation			0.055	104.7	192
Heater insulation			0.065	1046.6	240

3.4 NUMERICAL SIMULATION

Numerical simulation provides a method to visualize or predict the performance of a system under certain operating conditions. For heat and fluid flow in porous media, the number and type of equations to be solved depend on the rock properties, characteristics of the fluids, and process to be modeled. The independent primary variables that completely define the thermodynamic state of the flow system are pressure, temperature, and air mass fraction in single-phase flow, and they are temperature, pressure, and gas saturation in two-phase flow (Pruess, 1987).

In this section, the steps involved in modeling the vertical boiling experiment described in the previous chapter and estimating the two-phase parameters will be discussed. These steps include constructing a model, and carrying out forward and inverse calculations.

3.4.1 Model

A two-dimensional radial model of the vertical boiling experiment was constructed in TOUGH2, a numerical model for simulating the transport of water, steam, air, and heat in porous and fractured media (Pruess, 1991). The model has four concentric rings and 51 layers, where ring 1 is the innermost ring and layer 1 is the topmost layer (Fig. 3.6). From layer 1 to layer 44, ring 1 represents the core, ring 2 represents the epoxy, and ring 3 represents the core insulation. Layer 45 in ring 1 is the designated heater grid block, and it is further divided into five smaller elements to discretize the heat flow rate. Rings 2-3 in layer 45 represent the epoxy and core insulation, respectively. Layers 46-50, rings 1-3 are core insulation elements. Constant pressure boundary conditions were applied to all rings in layer 1 to maintain initial conditions at the top of the core, and to simulate water flowing out from the top of the core during the boiling process. The pressure at the boundary was equal to the measured pressure at the top end of the core. To model heat loss to the surroundings, ambient conditions were applied to all elements in ring 4 and layer 51. Grid blocks associated with constant pressure boundary and ambient conditions had very large volumes to ensure that their thermodynamic states remained constant in a simulation. An absolute permeability value was assigned only in the vertical direction

since fluid did not flow out in the radial direction. Initially, each grid block was at atmospheric temperature and pressure.

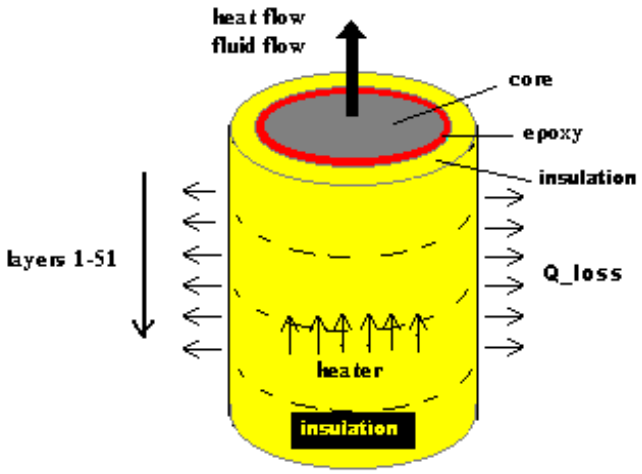

Figure 3.6 Schematic diagram of the 4×51 TOUGH2 model. Ring 4 is not shown since it represents ambient conditions.

3.4.2 Sensitivity Analysis

A sensitivity analysis was carried out in order to make reasonable initial guesses for the different parameters of interest and to better understand the system behavior. It was necessary to decouple the thermal parameters from the hydrogeologic parameters since the production of steam from liquid water in the experiments was highly dependent on the thermal properties of the materials and heat source. Thus, the thermal properties were studied under single-phase liquid conditions, while the hydrogeologic properties were studied under two-phase conditions.

Under single-phase liquid conditions, only temperature and heat flux were used to determine the effects of the thermal conductivity of each material. Temperature and heat flux profiles (with respect to the distance from the core) at five different times were generated for a base scenario. These were compared with results obtained from changing the thermal conductivity of each material one at a time. The results of the sensitivity analysis showed that temperature and heat flux were dependent on the heat losses from the heater, sandstone, and insulation materials under single-phase liquid conditions. Multiphase parameters affected the system only when two-phase conditions existed. They determined the temperature, pressure, and saturation distribution within the core, and the

upward propagation of steam. The observations made in the experiments were more sensitive to the steam relative permeability than to the liquid relative permeability.

3.4.3 Initial Guesses

To avoid time consuming inverse calculations, forward calculations were carried out and initial guesses were made. The initial guesses for α_s, α_i, and α_b were estimated by trial-and error, by changing each parameter one at a time. A rough fit of the temperature and heat flux data under single-phase conditions were obtained at α_s=4.930 W/m-C, α_i=0.150 W/m-C, and α_b=0.115 W/m-C, indicating heat losses. The linear relative permeability initial guesses were taken from the results obtained by Ambussso (1996). They are: S_{lr}=0.30, S_{gr}=0.10, S_{ls}=0.80 and S_{gs}=0.80. On the other hand, the initial guesses for the Brooks-Corey relative permeability parameters were obtained by trial-and-error, based on Satik's results (1998). S_{lr}=0.3, S_{gr}=0.1, and λ=1.5. For the Corey and van Genuchten relative permeability functions, the initial guesses for the residual saturations in the Brooks-Corey functions were used. Finally, the initial guesses for $P_{cmax,}$ p_e, p_o, and $1/\alpha$ were at 10^5 Pa, 2000 Pa, and 10^5, and 500 Pa, respectively.

3.5 PARAMETER ESTIMATION

3.5.1 Inverse Modeling

ITOUGH2 (Finsterle, 1997) provides inverse modeling capabilities for the TOUGH2 codes and solves the inverse problem by automatic model calibration based on the maximum likelihood approach. Figure 3.7 shows a flow chart of the inverse modeling process. TOUGH2 solves the forward problem and submits the results to ITOUGH2 during the calibration phase, when simulated data are compared with real data and the weighted difference between them is minimized. A higher accuracy of the model prediction can be achieved by a combined inversion of all available data since the different data types contribute to parameter estimation in different degrees (Finsterle et al, 1997). In this study, the observation data used were temperature, pressure, steam saturation, and heat flux. To obtain an aggregate measure of deviation between the observed and calculated system response, an objective function is introduced. In this case, the objective function is based on the standard weighting least square criterion, and it is given by

$$S = \mathbf{r}^T C_{zz}^{-1} \mathbf{r} \quad \text{..... (3.21)}$$

where $\mathbf{r}$ is the residual vector with elements $r_i = z_i^* - z_i(\boldsymbol{p})$, z_i^* is an observation (temperature, pressure, steam saturation, or heat flux) at a given point in time, z_i is the corresponding prediction that depends on the unknown parameters vector $\mathbf{p}$, and C_{zz} is the covariance matrix. The *ith* diagonal element of C_{zz} is the variance representing the measurement error. The objective function is minimized to be able to reproduce the observed system behavior more accurately. One way to reduce the objective function is to update $\mathbf{p}$ repeatedly to overcome the nonlinearity in $z_i(\mathbf{p})$. Finally a detailed error

analysis of the final residuals and the estimated parameters is conducted, under the assumption of normality and linearity (Finsterle et al., 1998). To compare the competing models, the *a posteriori* variance s_o^2, a goodness-of-fit measure, was used as a basis. It is given by

$$s_o^2 = \frac{\mathbf{r}^T \mathbf{C}_{yy}^{-1} \mathbf{r}}{M - N} \quad \text{..... (3.22)}$$

where M is the number of observations, and N is the number of parameters.

In preparing the ITOUGH2 input file, various information was required to describe the unknown parameters, measured data, and computational data. Successful inverse calculations depend on the data provided both in the TOUGH2 and ITOUGH2 input files. Details of the TOUGH2 file format can be found in Pruess (1987) and Pruess (1991), and details of the ITOUGH input file format can be found in Finsterle (1997).

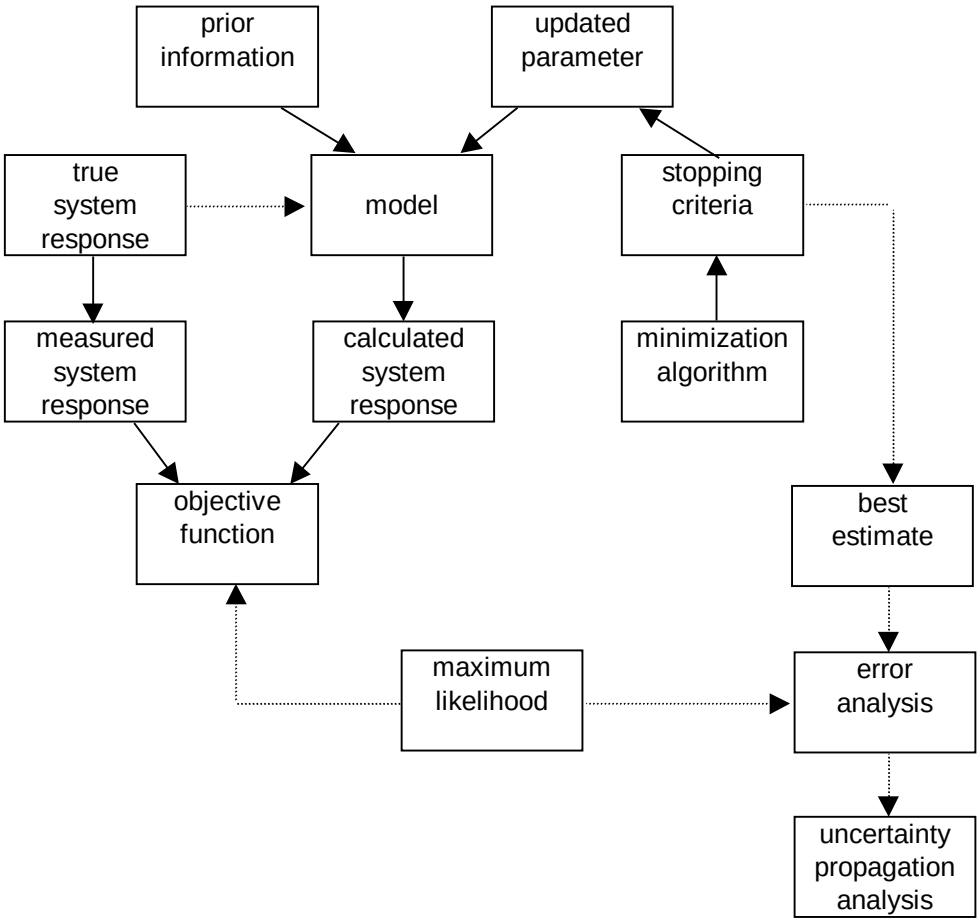

Figure 3.7 Inverse modeling flow chart (after Finsterle et al., 1998).

3.5.2 Results and Discussion

To reduce the correlation between parameters, the estimation process was divided into two parts: single-phase and two-phase periods. The thermal properties must be estimated in the absence of boiling, and multiphase parameters must be estimated under two-phase conditions. In the first half of the parameter estimation process, the heat flow rates (measured at five heat changes) H2-H6 were included with α_s, α_i, and α_b. The numerical model was calibrated against temperature and heat flux only since there were no pressure gradient and steam present. All temperature and heat flux data sets measured at 11 locations along the core were used in the single-phase period calibration.

The standard deviation values given in Table 3.2 reflect the uncertainty associated with the measurement errors. For heat flux, it is the standard deviation of the measured data only at Sensor 1, where the measurement uncertainty is larger than at any other observation point. The standard deviation at all other observation points was 10 W/m^2. Table 3.3 shows a summary of the estimated parameter set. The covariance and correlation matrices are given in Table 3.4, where the diagonal elements give the square of the standard deviation of the parameter estimate, σ_p. σ_p takes into account the uncertainty of the parameter itself and the influence from correlated parameters. In Table 3.5, the conditional standard deviation, σ_p* reflects the uncertainty of one parameter if all the other parameters are known. Hence, σ_p*/σ_p (column 3) is a measure of how independently a parameter can be estimated. A value close to one denotes an independent estimate, while a small value denotes strong correlation to other uncertain parameters. The total parameter sensitivity (column 4) is the sum of the absolute values of the sensitivity coefficients, weighted by the inverse of individual measurement errors and scaled by a parameter variation (Finsterle et al, 1997). As shown in Table 3.5, α_i and α_b are the most sensitive parameters. Except for H2 and H3, and perhaps H4, all parameters cannot be determined independently because they are correlated to one or more of the other parameters.

Table 3.2 Observation used for model calibration.

Data Type	Standard Deviation
Temperature	1 ^{o}C
Pressure	1000 Pa
Steam Saturation	0.01
Heat Flux	20 W/m^2

Table 3.3 Parameter estimates after single-phase calibration period.

Parameter	Initial Guess	Best Estimate
α_s, W/m-C	4.930	4.989
$\alpha\iota$, W/m-C	0.115	0.115
α_b, W/m-C	0.150	0.163
H2, W	0.234	0.190

H3, W	0.515	0.464
H4, W	0.972	0.994
H5, W	1.240	1.345
H6, W	1.510	1.679

Table 3.6 gives the statistical parameters related to the residuals. Comparing the total sensitivity of the two observation types, accurate measurements of temperature are sufficient to solve the inverse problem, i.e. heat flux data are much less sensitive. Also, the standard deviation values of the final residual are of the same order of magnitude as the measurement errors (Table 3.2). However, in the heat flux match in Figure 3.9, the random scattering around the diagonal line suggests that the matches to the individual sensors are not optimal in the least-square sense. The vertical distance of the symbol to the diagonal line represents the residual. The heat flux data show a systematic over- or under-prediction. Since this pattern is not observed in the temperature data (Figure 3.8), it is suspected that the heat flux sensors exhibit systematic trends. Moreover, the contribution of each observation type to the final value of the objective function (COF) is evenly distributed between temperature and heat flux, indicating that the choice of weighting factor is reasonable (Table 3.6). Although the *a posteriori* variance of 3 is not so much greater than one, the match could be improved by discarding some data, specifically at Sensor 1. The data at this location dominated the inverse calculation process that the estimates were such that they reflect more the observation at the boiling front, rather than the average two-phase condition in the core. Results of eliminating Sensor 1 data will be shown and analyzed later in this section.

Table 3.4 Variance-covariance matrix (diagonal and lower triangle) and correlation matrix (upper triangle) after single-phase period calibration.

	α_s	α_b	α_I	H2	H3	H4	H5	H6
α_s	1.37E-02	-3.87E-01	5.15E-01	1.25E-01	2.83E-01	5.42E-01	6.31E-01	6.49E-01
α_b	-1.32E-04	8.51E-06	-7.36E-01	-2.83E-01	-2.02E-01	-2.58E-01	-3.10E-01	-3.15E-01
α_i	9.00E-05	-3.20E-06	2.23E-06	1.25E-01	2.77E-01	5.27E-01	6.18E-01	6.27E-01
H2	1.43E-04	-8.05E-06	1.81E-06	9.50E-05	-1.07E-02	3.70E-02	4.12E-02	4.26E-02
H3	3.27E-04	-5.80E-06	4.07E-06	-1.03E-06	9.73E-05	1.32E-01	2.35E-01	2.37E-01
H4	7.27E-04	-8.61E-06	8.99E-06	4.12E-06	1.49E-05	1.31E-04	4.61E-01	4.95E-01
H5	1.01E-03	-1.23E-05	1.25E-05	5.46E-06	3.15E-05	7.17E-05	1.85E-04	5.58E-01
H6	1.27E-03	-1.53E-05	1.56E-05	6.90E-06	3.89E-05	9.43E-05	1.26E-04	2.77E-04

Table 3.5 Statistical measures and parameter sensitivity after single-phase period calibration.

Parameter	σ	σ^*/σ	Parameter Sensitivity
α_s	0.1172	0.6150	340
α_b	0.0029	0.5716	11872

α_i	0.0015	0.4380	43367
H2	0.0097	0.9468	1726
H3	0.0099	0.9410	1787
H4	0.0114	0.7604	1971
H5	0.0136	0.6602	1770
H6	0.0166	0.6415	1198

Table 3.6 Total sensitivity of observation, standard deviation of residuals, and contribution to the objective function (COF) after single-phase period calibration.

	Sensitivity	Standard Deviation	COF %
Temperature	2129	1.8	53.86
Heat Flux	567	16.6	45.93

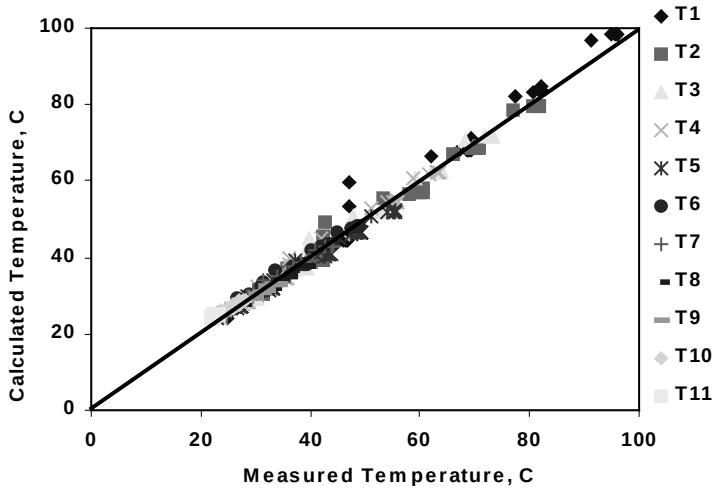

Figure 3.8 Measured and calculated temperature after single-phase period calibration.

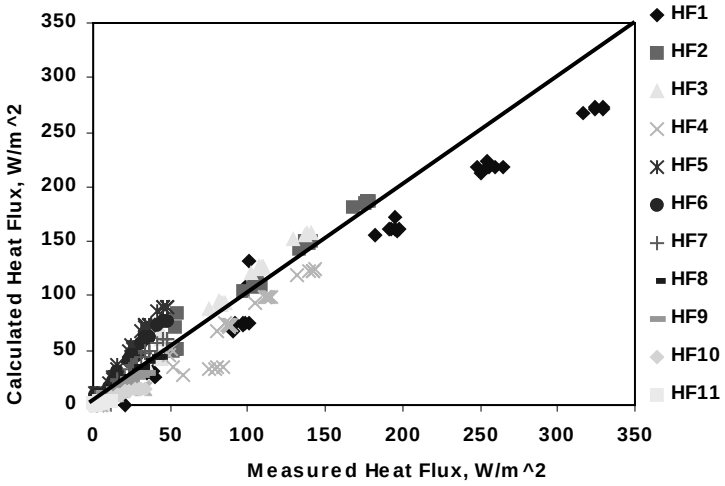

Figure 3.9 Measured and calculated heat flux after single-phase period calibration.

In the second part of the estimation process, the model was calibrated against temperature, pressure, steam saturation, and heat flux to estimate permeability, parameters of the different relative permeability and capillary pressure functions, and heat rate (H7 and H8) at the heat changes during the two-phase period. As observed in the first half of the estimation process, the heat rate estimates do not indicate a trend that only a fraction of the heat was actually going into the core (Table 3.11). If this were not so, the heat rate could have been discarded in the second half of the estimation process, eliminating the correlation between the heat input and the two-phase parameters. The absolute permeability was included as an unknown since it is also a fluid flow property. Whereas all 11 sets of temperature, pressure, and heat flux were employed, only six sets of steam saturation data were used. This was because the two-phase region was confined within the first 7 cm from the heater. Considering only these data reduced the error in the calculation. The apparent two-phase region observed under single-phase conditions was probably due to density differences in the liquid water, with the liquid closer to the heater having a smaller density, and not because steam was actually present. Thus, a simple linear correction was applied to minimize unreasonable steam saturation values during the single-phase period. To reduce the error variance both single- and two-phase data were employed in the second half of the inversion process. However, many calibration points were wasted in that the model had already been previously calibrated using single-phase data.

Subjecting all competing models to the two-phase parameter estimation process, the model that gave the smallest error variance, S_o^2, was the linear capillary relative permeability and Leverett capillary pressure case. However, S_o^2=6.4 is significantly greater than one and it reflects the fact that the match is not as good as expected. This is partly due to the inaccurate estimates of the thermal properties and heat rates in the first part of the estimation process, and partly because of the constraints posed by the large number of parameters being estimated at the same time. The error variance of the other

estimates were of the same order of magnitude as the error variance of the linear relative permeability and Leverett capillary pressure case, although the models differ from each other. Thus, using the error variance as a goodness-of-fit criterion, none of the cases performs significantly better than the others. However, as suggested earlier, the function that matches the data without over-parameterization is the most likely scenario.

Table 3.7 shows a summary of the estimated parameter set for the linear relative permeability and Leverett capillary pressure case. Results show that S_{gr} and S_{gs} are the most sensitive parameters. Except for *k*, S_{ls}, and *H7*, all parameters cannot be determined independently because they are correlated to one or more of the other parameters (Table 3.9). Of particular interest are the very low values of σ^*/σ for S_{gr}, S_{gs}, and P_o. This implies that they are highly correlated with one another or with the other parameters. Comparing the total sensitivity of all observation types (Table 3.10), accurate measurements of temperature, pressure, and steam saturation are sufficient to solve the inverse problem. Although the standard deviation values of the final residual are of the same order of magnitude as the measurement errors (Table 3.2), the assumed accuracy of the match was overestimated. The standard deviation of the steam saturation residual is greater than the error measurement by an order of magnitude. This shows clearly that there was a systematic deviation in the steam saturation match. This could be due to the fact that the steam saturation was measured only three times during the two-phase period. During the calibration phase, steam saturation data were just interpolated between the three measured data points. Since the parameters are highly sensitive to the steam saturation, slight errors in the steam saturation data could be translated to greater errors in the predictions. Also, the corrections applied to the steam saturation data may have a great bearing on the estimates. As in the first half of the estimation process, the heat flux match in Figure 3.13. has random scattering around the diagonal line, suggesting that the matches to the individual sensors are not optimal in the least-square sense. Since the under- and over-prediction pattern is not observed in the temperature data (Figure 3.10), the heat flux sensors may exhibit systematic trends. Furthermore, the pressure during the two-phase period is under-predicted (Fig. 3.11). It may be due to the insufficient capillary pressure predicted by the Leverett function. The contribution of each observation type to the final value of the objective function (COF) is well balanced (Table 3.10). Figures 3.14-3.17 show the predicted and measured temperature, pressure, steam saturation, and heat flux in terms of time, respectively. Figures 3.18-3.21 show the predicted and measured temperature, pressure, steam saturation, and heat flux in terms of distance from the heater.

Table 3.7 Parameter estimates for linear relative permeability and Leverett capillary pressure case.

Parameter	Initial Guess	Best Estimate
S_{lr} (RP)	0.30	0.33
S_{gr}	0.10	0.16
S_{ls}	0.80	0.82

S_{gs}	0.80	0.92
P_o	100,000	92,941
S_{lr} (CP)	0.30	0.12
k, md	780	3080

Table 3.8 Variance-covariance and correlation matrices.

	k	S_{lr} (RP)	S_{gr}	S_{ls}	S_{gs}
K	3.04E-06	-4.60E-02	6.98E-02	-2.82E-03	-2.83E-02
S_{lr} (RP)	-5.79E-07	5.21E-05	-5.91E-01	-3.16E-01	-3.16E-01
S_{gr}	3.77E-07	-1.32E-05	9.56E-06	-3.51E-02	4.69E-01
S_{ls}	-6.16E-07	-2.86E-04	-1.36E-05	1.57E-02	4.56E-02
S_{gs}	-1.45E-07	-6.68E-06	4.24E-06	1.67E-05	8.56E-06
P_o	-2.18E-06	2.61E-05	-2.16E-05	1.52E-04	1.81E-05
S_{lr} (CP)	-3.20E-07	-8.43E-06	-1.01E-05	-1.25E-05	6.79E-06
HR7	-1.04E-07	4.23E-06	-2.85E-06	4.61E-06	-5.16E-07
HR8	6.01E-08	1.04E-05	-3.99E-06	8.99E-06	-1.84E-06

	P_o	S_{lr} (CP)	HR7	HR8
k	-9.70E-02	-2.26E-02	-2.54E-02	1.26E-02
S_{lr} (RP)	2.80E-01	-1.44E-01	2.50E-01	5.24E-01
S_{gr}	-5.44E-01	-4.03E-01	-3.94E-01	-4.70E-01
S_{ls}	9.43E-02	-1.23E-02	1.57E-02	2.62E-02
S_{gs}	4.82E-01	2.86E-01	-7.53E-02	-2.29E-01
P_o	1.66E-04	6.57E-01	3.19E-01	2.79E-01
S_{lr} (CP)	6.85E-05	6.58E-05	1.98E-01	-5.45E-02
HR7	9.61E-06	3.75E-06	5.48E-06	2.03E-01
HR8	9.86E-06	-1.21E-06	1.31E-06	7.53E-06

Table 3.9 Statistical measures and parameter sensitivity.

Parameter	σ	σ*/σ	Parameter Sensitivity
k	0.0017	0.9893	8109
S_{lr} (RP)	0.0072	0.5025	6222
S_{gr}	0.0031	0.0820	40215
S_{ls}	0.1253	0.7989	152
S_{gs}	0.0029	0.0866	30669

P_o	0.0129	0.0835	9632
S_{lr} (CP)	0.0081	0.5144	7579
HR7	0.0023	0.9097	7172
HR8	0.0027	0.7366	8964

Table 3.10 Total sensitivity of observation, standard deviation of residuals, and contribution to the objective function (COF).

Observation	Sensitivity	Standard Deviation	COF %
Temperature	1041	1.9 C	14.54
Pressure	3383	1740 Pa	16.98
Saturation	6783	0.09	37.84
Heat Flux	311	28.1 W/m^2	30.64

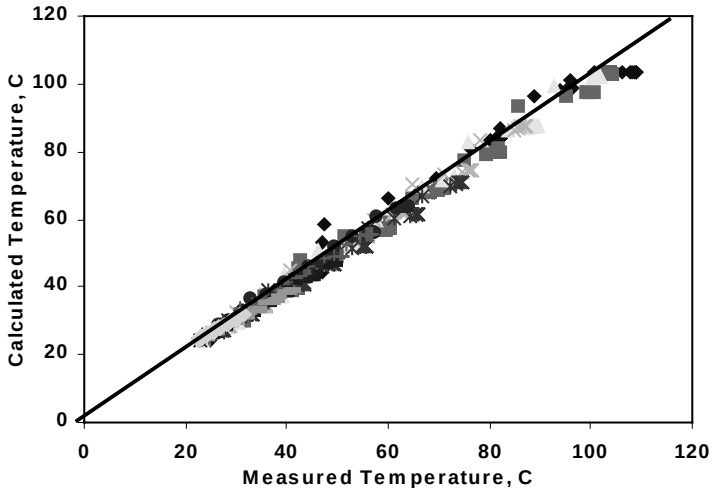

Figure 3.10 Measured and calculated temperature.

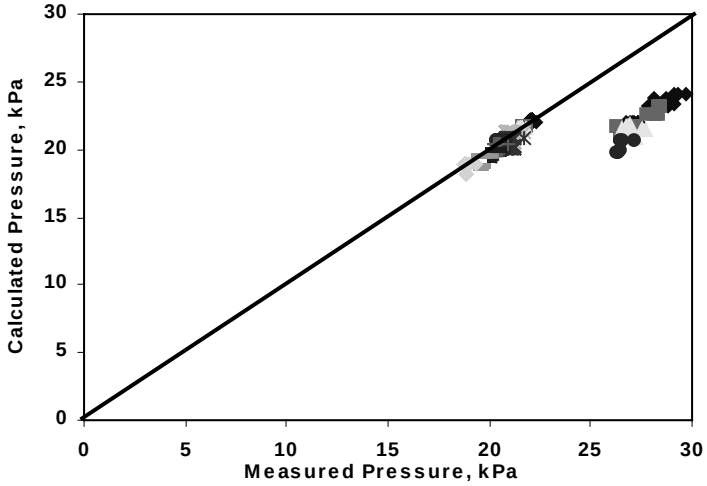

Figure 3.11 Measured and calculated pressure.

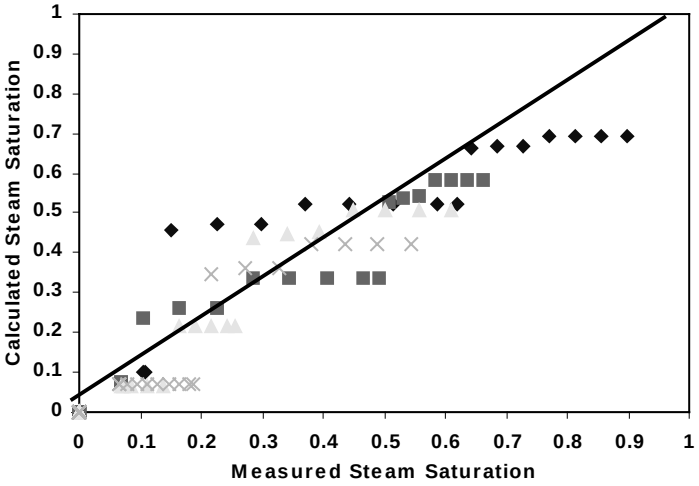

Figure 3.12 Measured and calculated steam saturation.

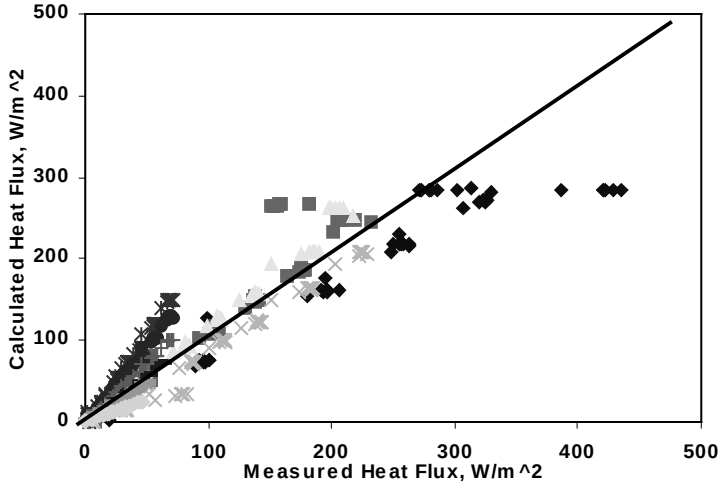

Figure 3.13 Measured and calculated heat flux.

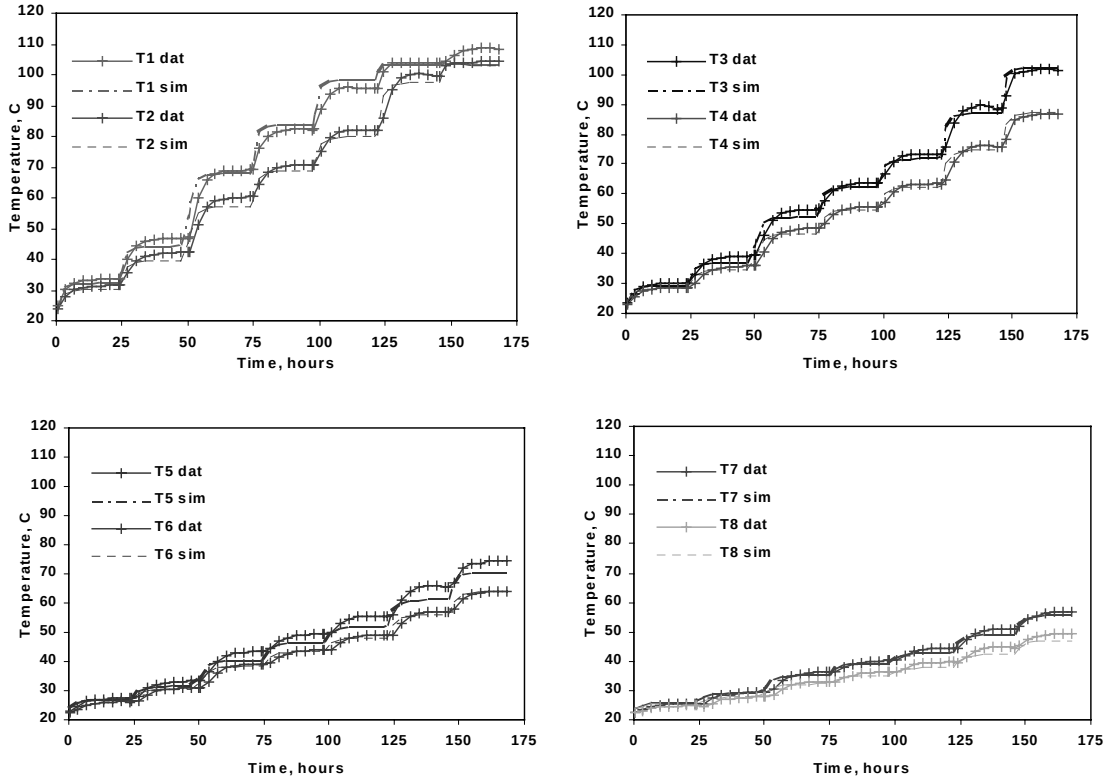

Figure 3.14 Temperature with respect to time.

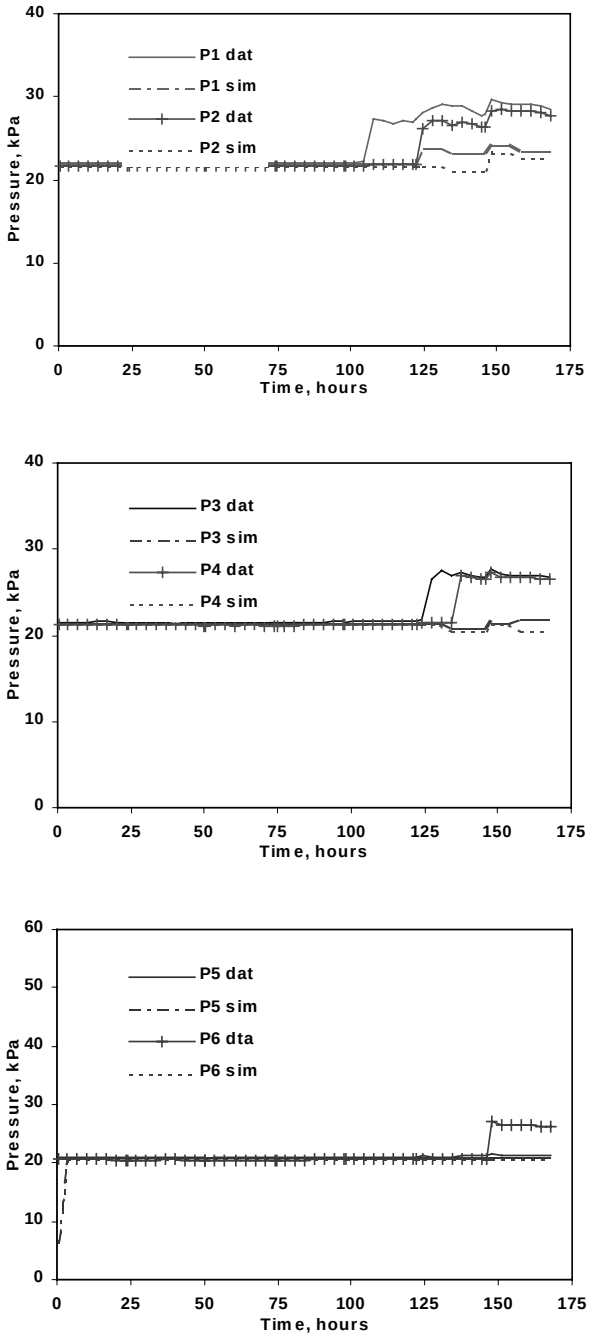

Figure 3.15 Pressure with respect to time.

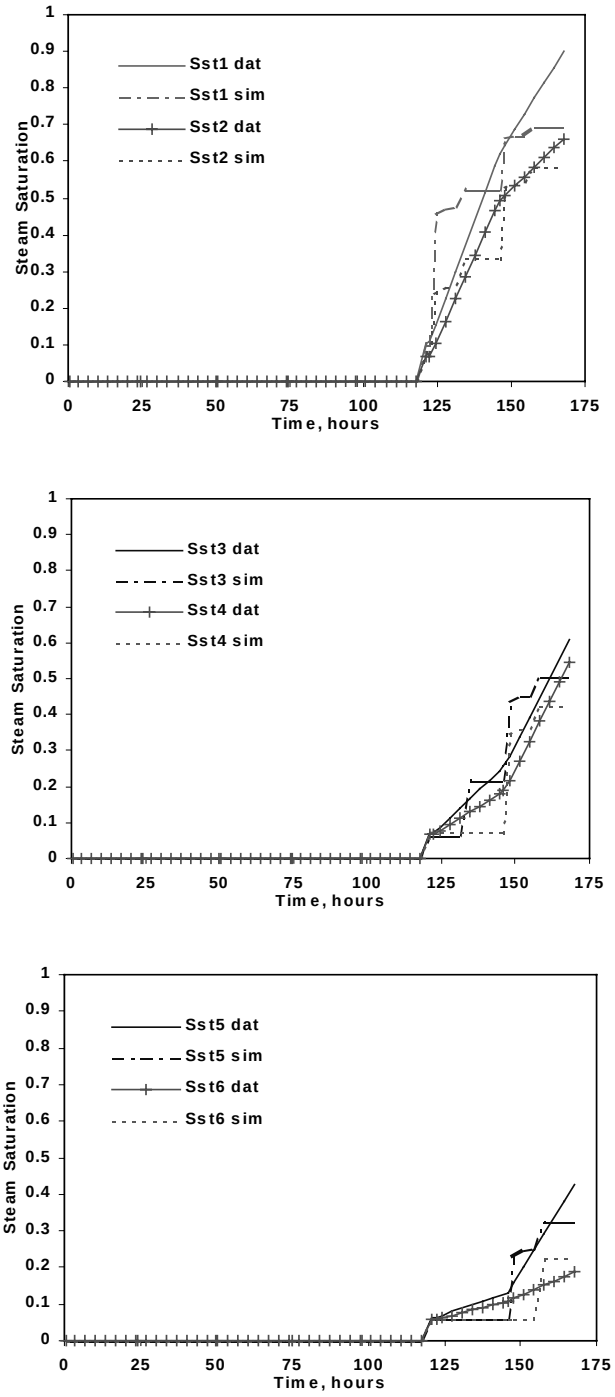

Figure 3.16 Steam saturation with respect to time.

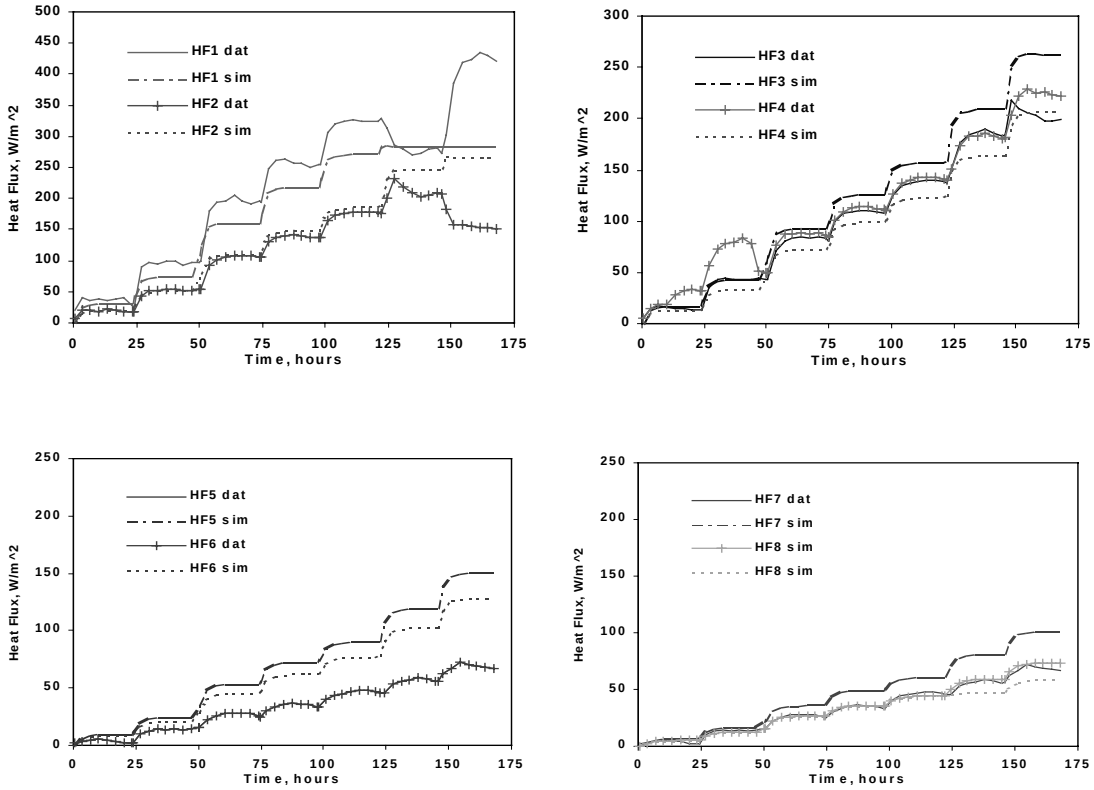

Figure 3.17 Heat flux with respect to time.

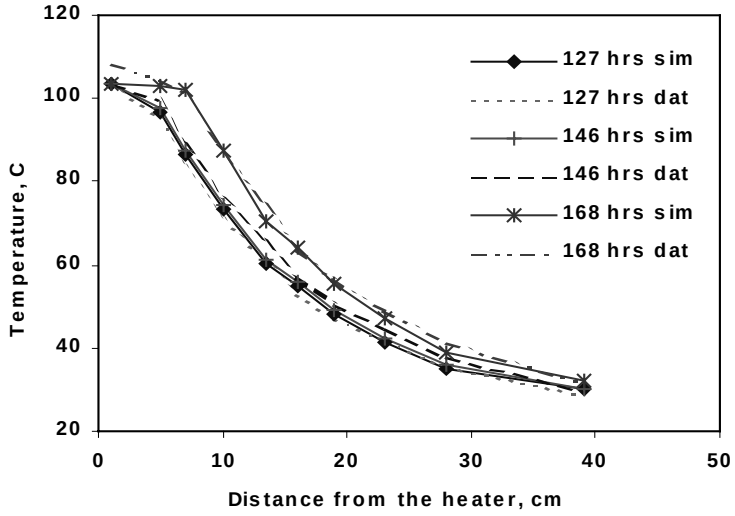

Figure 3.18 Temperature with respect to distance from the heater.

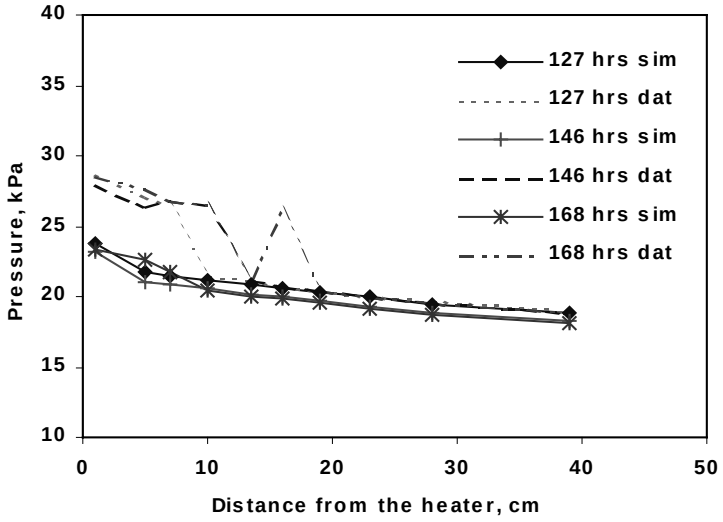

Figure 3.19 Pressure with respect to distance from the heater.

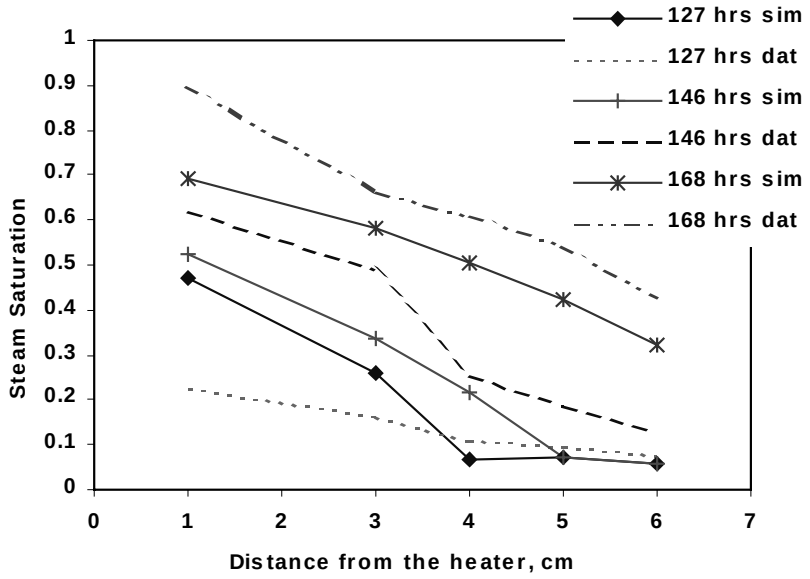

Figure 3.20 Steam saturation with respect to distance from the heater.

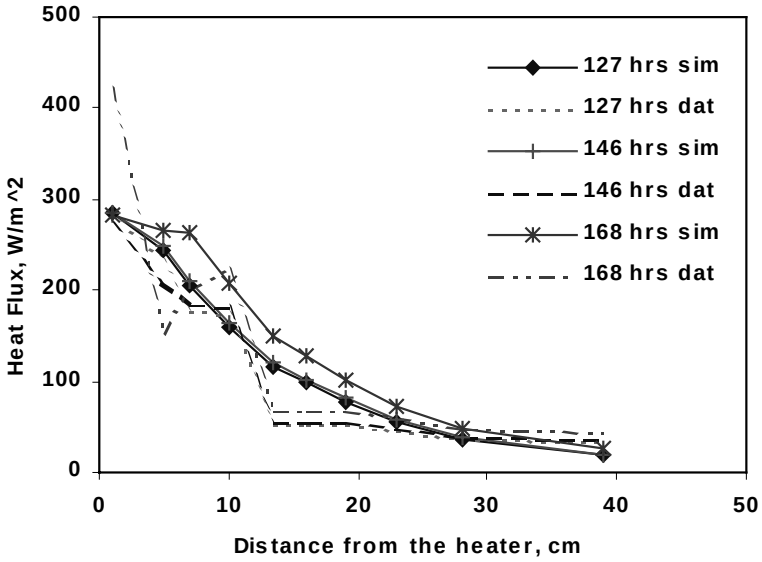

Figure 3.21 Heat flux with respect to distance from the heater.

Figure 3.22 shows the linear relative permeability curves based on the two-phase parameter estimates and Figure 3.23 shows the corresponding Leverett capillary pressure. The liquid relative permeability agrees well with Ambusso's results. On the other hand, S_{gl} does not coincide with the measured S_{gl}, although there is a good agreement between the estimated S_{gr} and Ambusso's k_{gr}. Figure 5.24 shows the relative permeability estimates obtained from the estimation process. Although the relative permeability relations of the models are different, they all seem to agree in terms of S_{gr}. The S_{gr} value is around 0.15-0.20. Since the observations made during the boiling experiment were more sensitive to the steam relative permeability, inverse modeling at least made S_{gr} consistent. A comparison of the different relative permeability estimates with the results obtained by Satik is also shown in Figure 3.25. Although Corey's relative permeability (estimates from the Corey relative permeability and linear capillary pressure case) best mimic Satik's curves, the fit was worse than that obtained from the linear relative permeability and Leverett capillary pressure case.

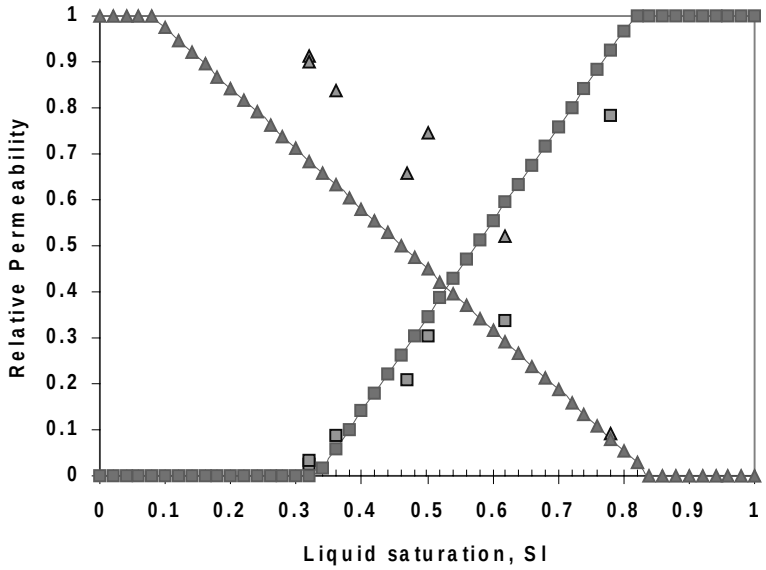

Figure 3.22 Inverse modeling relative permeability results compared with Ambusso's results (1996).

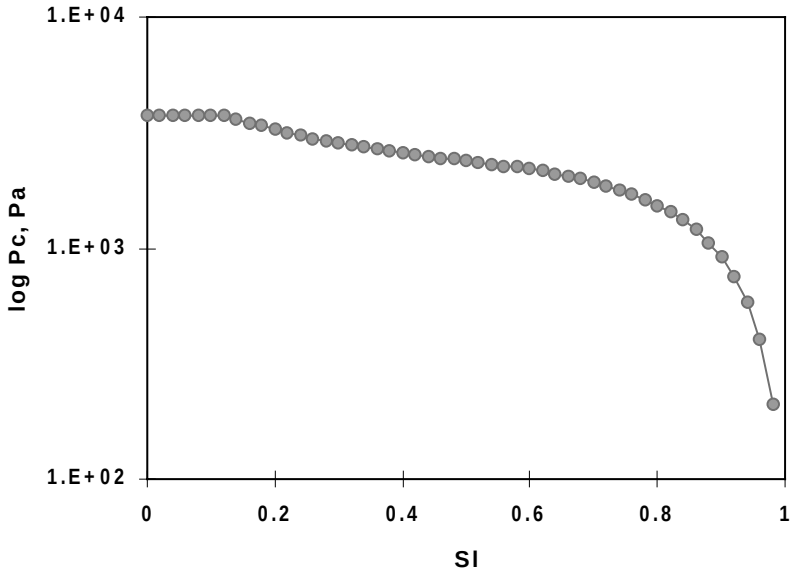

Figure 3.23 Leverett capillary pressure.

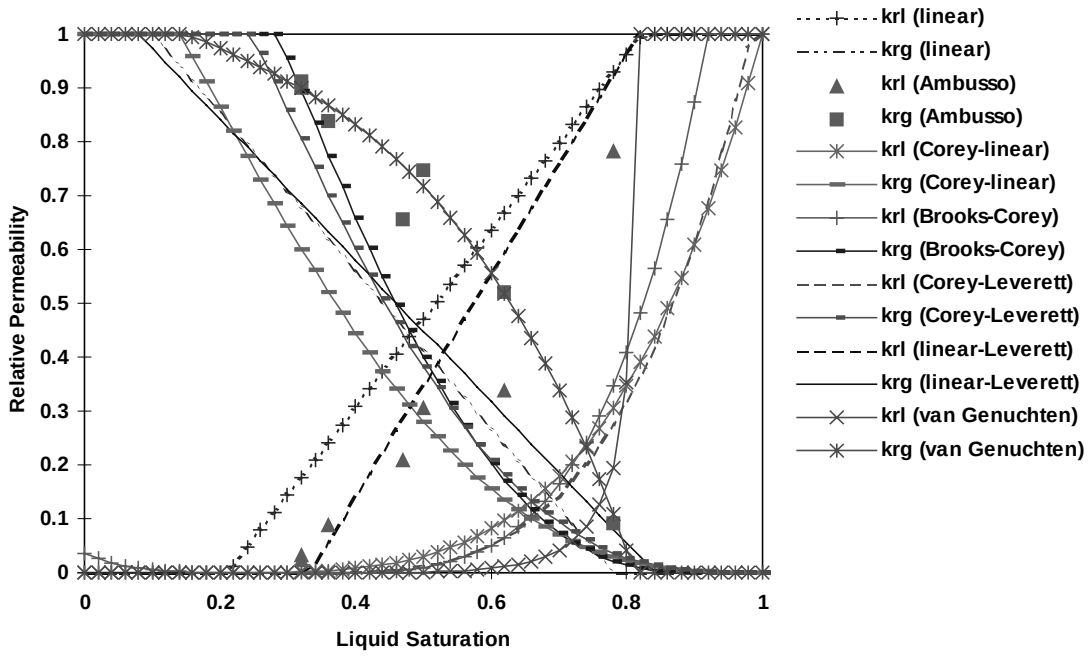

Figure 3.24 Relative permeability estimates compared with Ambusso's (1996) results.

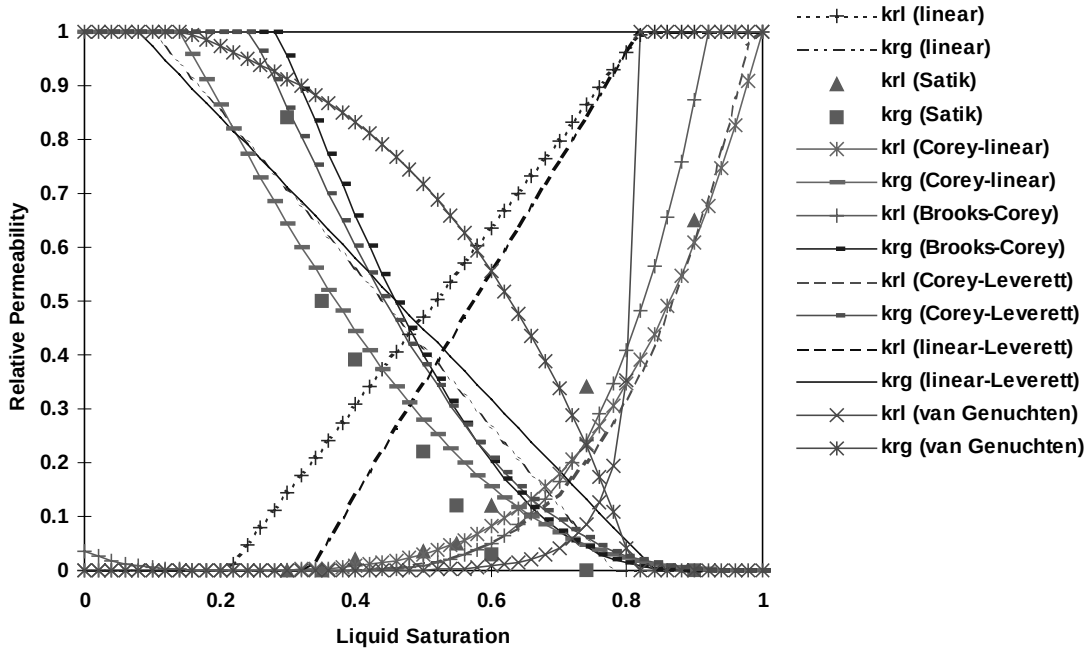

Figure 3.25 Relative permeability estimates compared with Satik's (1996) results.

The error variance, S_o^2, can be improved by discarding some observation data. Since data at Sensor 1 dominated the estimation process, it is practical to eliminate them. By doing so, the error caused by the heat input, boundary effects, and adsorption can be minimized. Also, the effects of the poorly understood capillary pressure of superheated steam can be

reduced. Going through the same parameter estimation process, S_o^2 was reduced to 1.9 after the single-phase calibration period. Although this is still greater than one, it gave a better fit than the previous estimates (with Sensor 1 data). Table shows the parameter estimates after the single-phase calibration period. As expected, the estimates for the thermal properties and heat input are lower than in the previous case since data from Sensor 1 were not included in the calibration period. The most sensitive parameters are α_i and $\alpha_{b,}$ which concurs with the finding in the previous estimation process. Except for H4, H5, and H6, none of the parameters can be estimated independently without high uncertainty (Table 3.12). Comparing the total sensitivity of the different observation types (Table 5.13), accurate measurements of temperature are sufficient to solve the inverse problem. Moreover, the standard deviation values of the final residual (Table 3.13) are of the same order of magnitude as the measurement errors, although the heat flux matches to the individual sensors are not optimal in the least square sense (Fig. 3.27). Finally, the contribution of temperature and heat flux to the final value of the objective function is well balanced (Table 3.13).

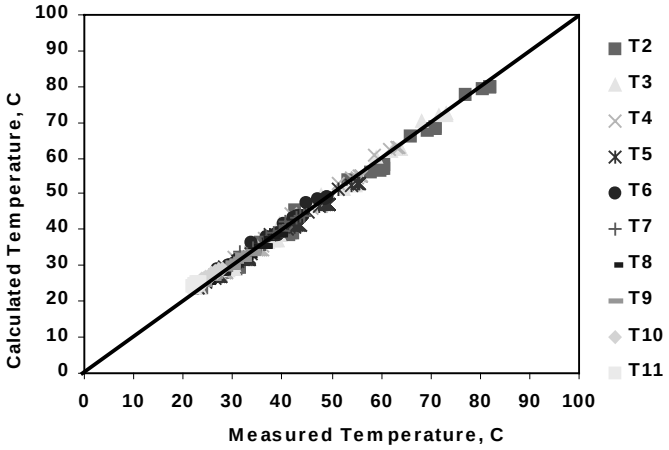

Figure 3.26 No Sensor 1 data: Measured and calculated temperature after calibration of model under single-phase conditions.

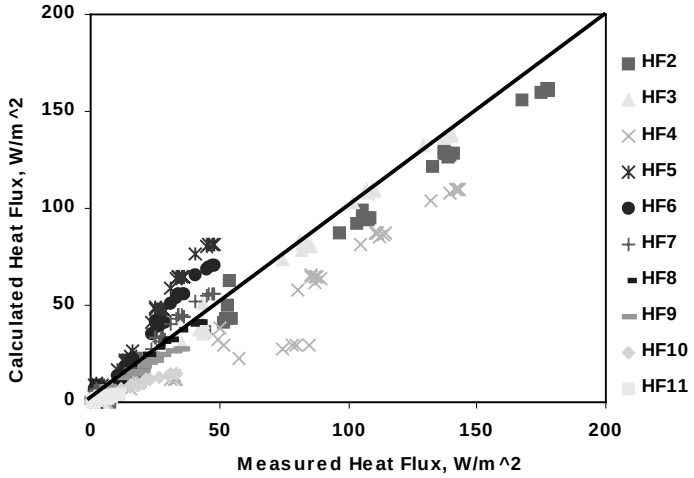

Figure 3.27 No Sensor 1 data: measured and calculated heat flux after calibration of model under single-phase conditions.

Table 3.11 No Sensor 1 data: Parameter estimates after the single-phase calibration period.

Parameter	Initial Guess	Best Estimate
α_s	4.930	4.826
α_b	0.150	0.066
α_i	0.115	0.100
HR2	0.235	0.141
HR3	0.515	0.482
HR4	0.972	0.802
HR5	1.237	1.079
HR6	1.510	1.357

Table 3.12 No Sensor 1 data: Variance-covariance and correlation matrices after single-phase period calibration.

	α_s	α_b	α_i	HR2	HR3	HR4	HR5	HR6
α_s	1.48E-02	-5.69E-01	4.01E-01	1.14E-01	1.54E-01	2.32E-01	2.94E-01	2.85E-01
α_b	-3.29E-04	2.26E-05	-5.86E-01	-7.74E-01	-2.45E-01	-3.81E-02	-5.21E-02	-5.46E-02
α_i	6.95E-05	-3.98E-06	2.04E-06	1.91E-01	3.06E-01	5.03E-01	6.14E-01	5.55E-01
HR2	1.08E-04	-2.89E-05	2.14E-06	6.15E-05	-2.56E-01	-2.38E-01	-2.83E-01	-2.55E-01
HR3	1.56E-04	-9.74E-06	3.65E-06	-1.68E-05	7.00E-05	1.26E-01	1.56E-01	1.42E-01
HR4	2.61E-04	-1.68E-06	6.64E-06	-1.72E-05	9.78E-06	8.55E-05	4.44E-01	3.37E-01
HR5	4.18E-04	-2.91E-06	1.03E-05	-2.60E-05	1.53E-05	4.81E-05	1.37E-04	4.69E-01
HR6	4.44E-04	-3.33E-06	1.01E-05	-2.57E-05	1.53E-05	3.99E-05	7.04E-05	1.64E-04

Table 3.13 No Sensor 1 data: Statistical measures and parameter sensitivity after single-phase period calibration.

Parameter	σ	σ^*/σ	Parameter Sensitivity
α_s	0.1215	0.0656	1129
α_b	0.0048	0.0231	74231
α_i	0.0014	0.1163	74700
HR2	0.0078	0.0295	34257
HR3	0.0084	0.0695	14404
HR4	0.0092	0.7539	2081
HR5	0.0117	0.6369	1758
HR6	0.0128	0.7040	1080

Table 3.14 No Sensor 1 data: Total sensitivity of observation, standard deviation of residuals, and contribution to the objective function (COF) after single-phase period calibration.

	Sensitivity	Standard Deviation	COF %
Temperature	10350	1.4	54.42
Heat Flux	2684	13.1	44.54

Subjecting all competing models to the two-phase parameter estimation process, the model that gave the smallest error variance, S_o^2, was the linear capillary relative permeability and capillary pressure model. Although the error variance was reduced as a result of not including data at Sensor 1, S_o^2=5.2 is still significantly greater than one. Thus, the match is not as good as expected. This is in part due to the inaccurate estimates of the thermal properties and heat rates in the first part of the estimation process, and

partly because of the constraints posed by the large number of parameters being estimated at the same time. The error variance values of the other estimate were of the same order of magnitude as the error variance of the linear relative permeability and capillary pressure case. This indicates that none of the cases performs significantly better than the others, although each model is different from another.

Table 3.15 shows a summary of the estimated parameter set for the linear model. Results show that k, HR8, HR7, and S_{gr} are the most sensitive parameters, and S_{lr} and S_{ls} are not sensitive parameters at all (Table 3.17). This means that S_{lr} and S_{ls} can assume any value and not affect the inversion process. Except for k, S_{lr}, and S_{ls}, all parameters cannot be determined independently because they are correlated to one or more of the other parameters. Although the standard deviation values of the final residual (Table 3.18) are of the same order of magnitude as the measurement errors (Table 3.2), the assumed accuracy of the match was overestimated. The large standard deviation of the steam saturation residual shows that there was a systematic mismatch to in the steam saturation measurements. Furthermore, the pressure during the two-phase period is under-predicted (Fig. 3.29). It may be due to the insufficient capillary pressure predicted by the linear function, although it is greater than the one predicted in the previous case. The heat flux matches in Figure 3.31 has an under- and over-prediction pattern that is not observed in the temperature match (Figure 3.28). This indicates that the heat flux sensors may exhibit systematic trends. In addition, the contribution of each observation type to the objective function is well balanced. Figures 3.32-3.35 show the predicted and measured temperature, pressure, steam saturation, and heat flux in terms of time, respectively. Figures 3.36-3.39 show the predicted and measured temperature, pressure, steam saturation, and heat flux in terms of distance from the heater. Clearly, the fit is better than in the previous case.

Figure 3.40 shows a comparison of the relative permeability obtained by Ambusso (1996) and by inverse calculation. As in the previous case, the two relative permeability relation agree on S_{gr}. S_{lr} and S_{ls} can be manipulated to coincide with Ambusso's results since the observation data are not sensitive to them. Figures 3.42 and 3.43 show a comparison of all the models with Ambusso's results and Satik's measurements, respectively. Except for the van Genuchten model, all models agree on the value of S_{gr} which is around 0.1.

In general, the inverse problem that was formulated here was ill-posed since too many parameters were estimated at the same time. This could not be avoided, however, since the thermal parameters, including the heat input, were strongly correlated with the hydrogeologic properties. This was due to the fact that the two-phase flow was driven only by boiling, and not by, say, fluid injection. Thus, it was necessary to divide the estimation process into two parts: single-phase and two-phase period estimation. This reduced the dependence between the multiphase and thermal parameters, although not completely. If the thermal parameters and capillary pressure were known, a more accurate estimate of the relative permeability could be achieved. However, this was not possible under the given operating conditions. Consequently, the results of the estimation process

were ambiguous, making the determination of the appropriate relative permeability as well as the capillary pressure function difficult.

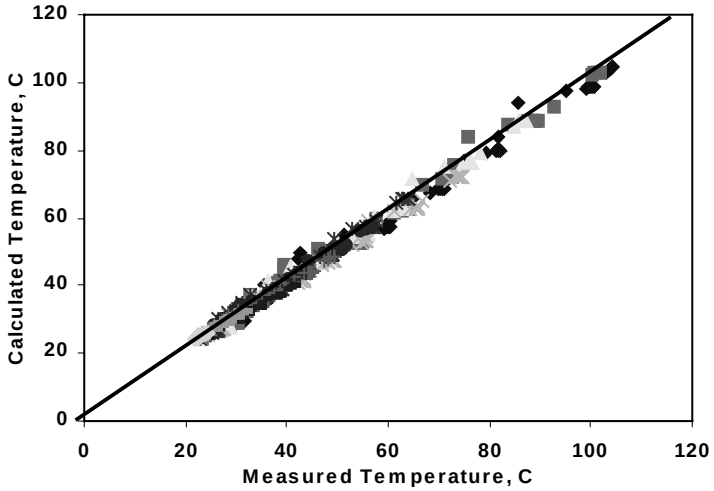

Figure 3.28 No Sensor 1 data: Measured and calculated temperature.

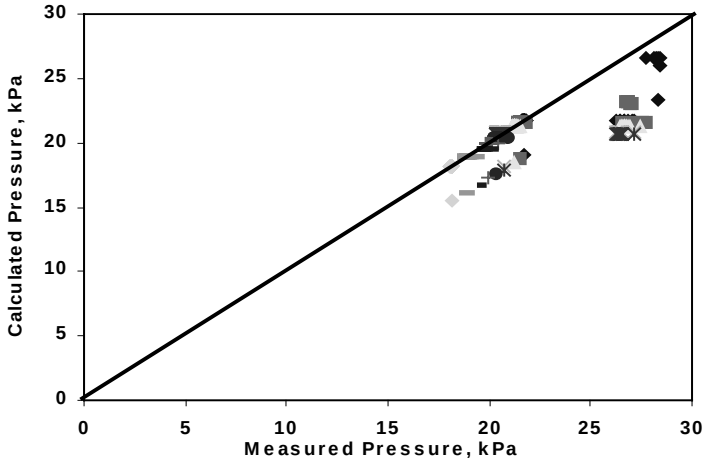

Figure 3.29 No Sensor 1 data: Measured and calculated pressure.

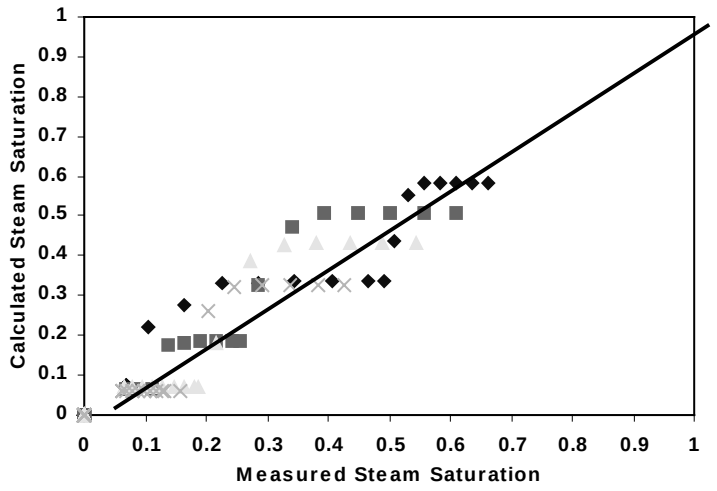

Figure 3.30 No Sensor 1 data: Measured and calculated steam saturation.

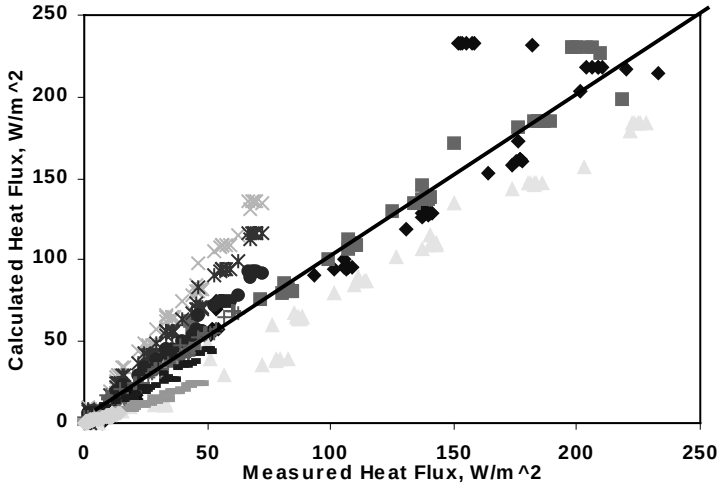

Figure 3.31 No Sensor 1 data: Measured and calculated heat flux.

Table 3.15 No Sensor 1 data: Parameter estimates.

Parameter	Initial Guess	Best Estimate
k, md	780	518
S_{lr}	0.30	0.31
S_{gr}	0.10	0.10
S_{ls}	0.80	0.80
S_{gs}	0.80	1.00
P_{cmax}, Pa	100000	12,788
HR7, W	1.790	1.729
HR8, W	2.083	2.005

Table 3.16 No Sensor 1 data: Variance-covariance and correlation matrices.

	k	S_{lr}	S_{gr}	S_{ls}	S_{gs}	P_{cmax}	HR7	HR8
k	3.65E-07	5.38E-05	-4.48E-05	5.82E-05	4.82E-03	-7.75E-03	-1.38E-03	-1.90E-03
S_{lr}	3.70E-09	1.30E-02	1.68E-02	-6.57E-04	-5.68E-03	1.16E-02	-7.99E-03	-1.71E-03
S_{gr}	-4.49E-10	3.17E-05	2.76E-04	1.70E-02	-3.75E-03	4.33E-01	-7.52E-01	-7.18E-01
S_{ls}	4.00E-09	-8.52E-06	3.21E-05	1.30E-02	-6.18E-03	1.62E-02	-5.38E-03	-4.11E-03
S_{gs}	2.67E-07	-5.94E-05	-5.72E-06	-6.46E-05	8.44E-03	8.61E-01	1.57E-01	2.13E-01
P_{cmax}	-2.24E-07	6.33E-05	3.43E-04	8.80E-05	3.78E-03	2.28E-03	-1.51E-01	-3.21E-02
HR7	-2.46E-09	-2.69E-06	-3.69E-05	-1.81E-06	4.27E-05	-2.13E-05	8.71E-06	6.33E-01
HR8	-3.03E-09	-5.13E-07	-3.14E-05	-1.23E-06	5.16E-05	-4.04E-06	4.92E-06	6.95E-06

Table 3.17 No Sensor 1 data: Total sensitivity of observation, standard deviation of residuals, and contribution to the objective function (COF).

Parameter	σ	σ^*/σ	Parameter Sensitivity
k	0.0006	0.9986	13396
S_{lr}	0.1139	0.9992	5
S_{gr}	0.0166	0.2869	3598
S_{ls}	0.1139	0.9982	6
S_{gs}	0.0919	0.2552	596
P_{cmax}	0.0478	0.2141	1536
HR7	0.0030	0.6208	7057
HR8	0.0026	0.5513	11425

Table 3.18 No Sensor 1 data: Total sensitivity of observation, standard deviation of residuals, and contribution to the objective function (COF).

	Sensitivity	Standard Deviation	COF %
Temperature	4.79E+02	1.67	21.11
Pressure	2.48E+03	1410	13.36
Saturation	2.41E+03	0.067	40.64
Heat flux	1.39E+02	19.8	24.67

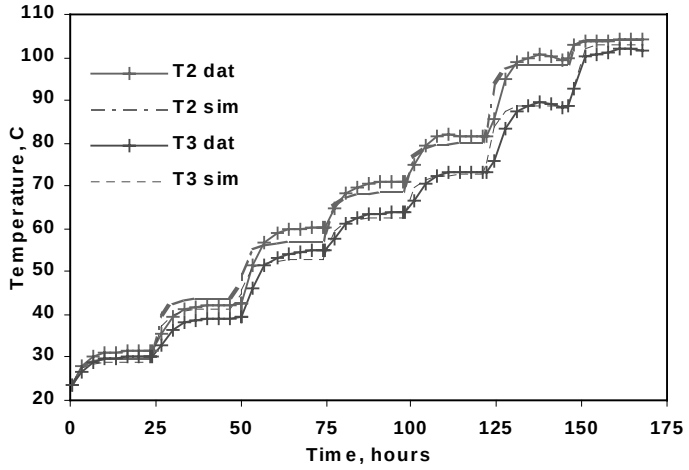

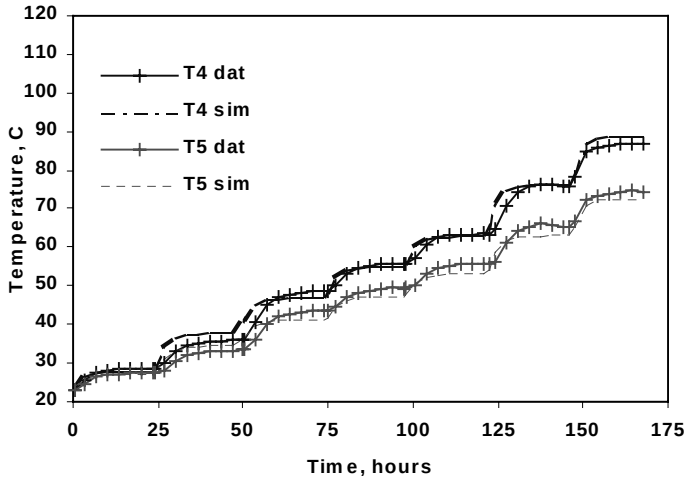

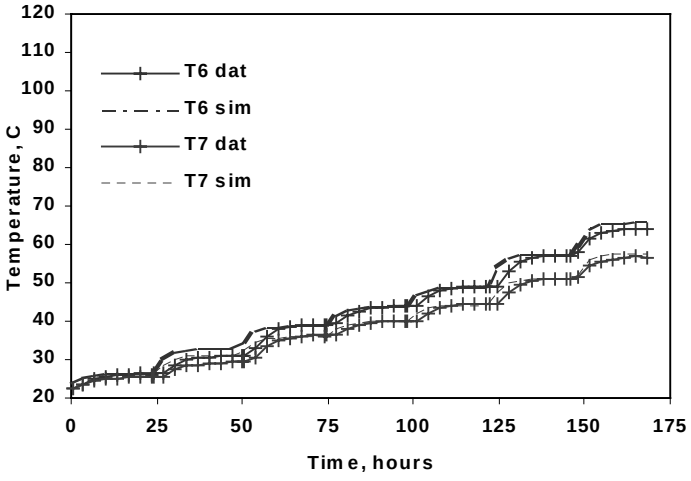

Figure 3.32 No Sensor 1 data: Temperature with respect to time.

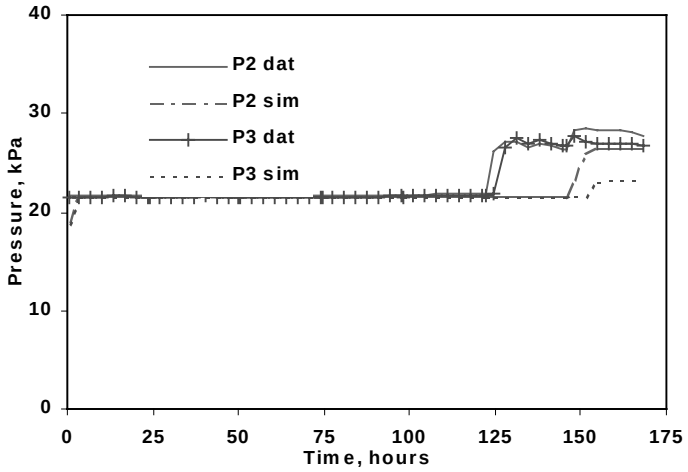

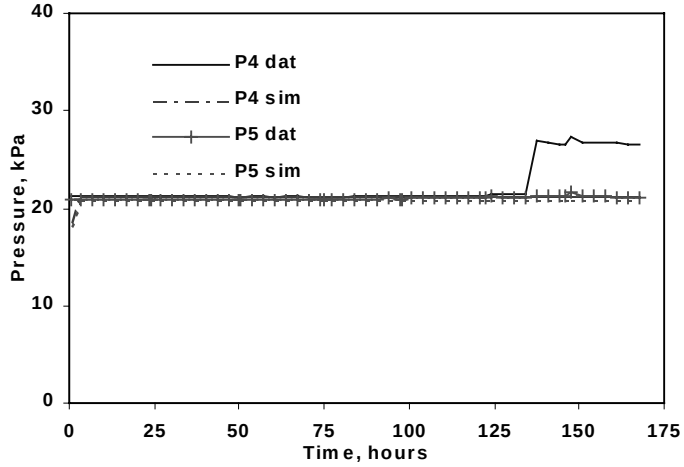

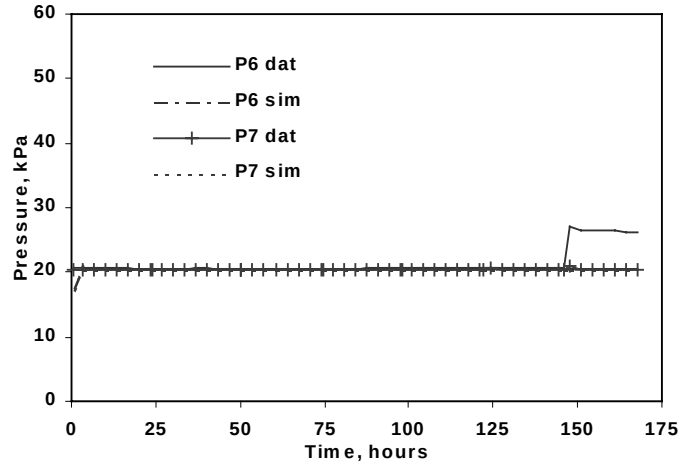

Figure 3.33 No Sensor 1 data: Pressure with respect to time.

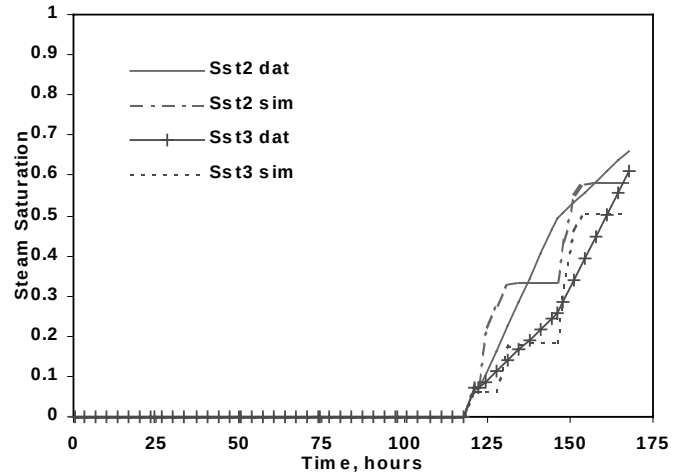

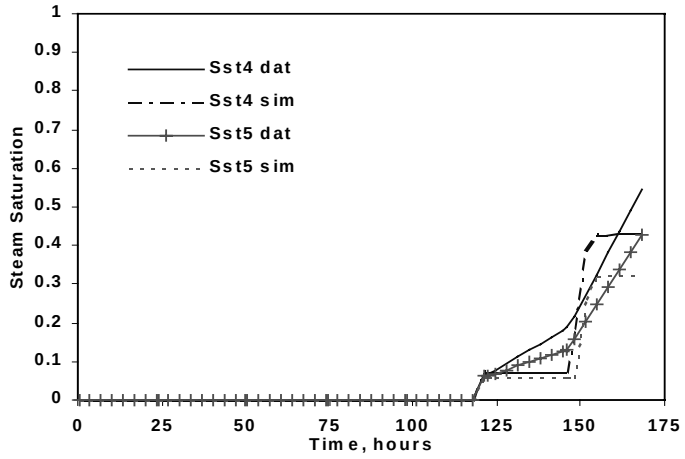

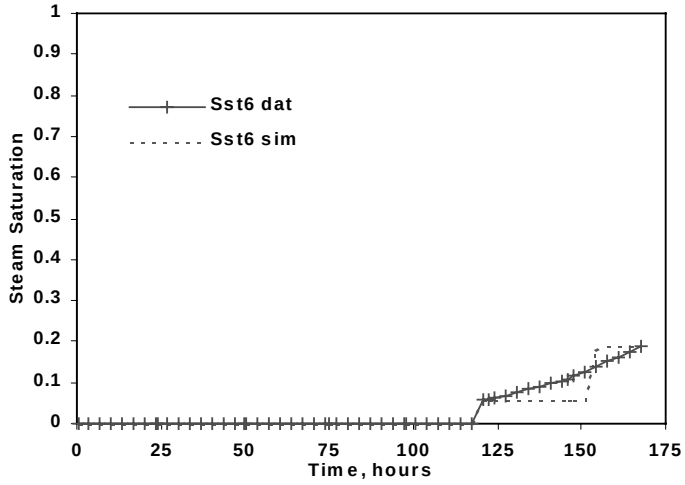

Figure 3.34 No Sensor 1 data: Steam saturation with respect to time.

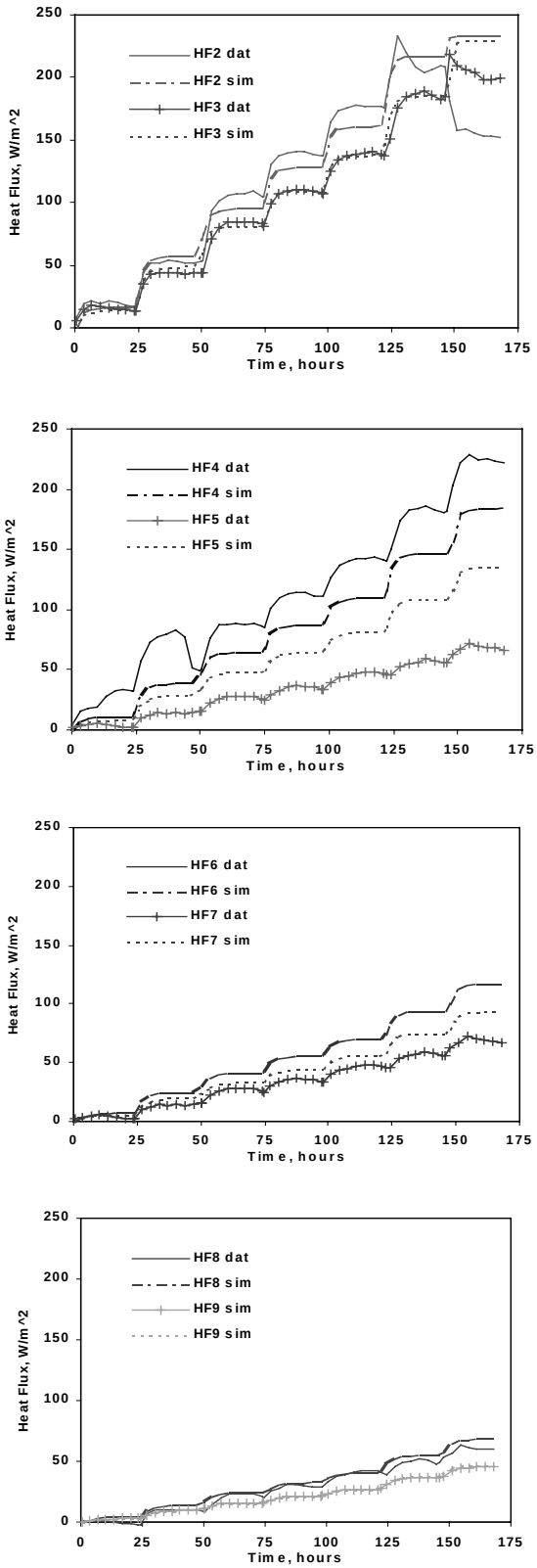

Figure 3.35 No Sensor 1 data: Heat flux with respect to time.

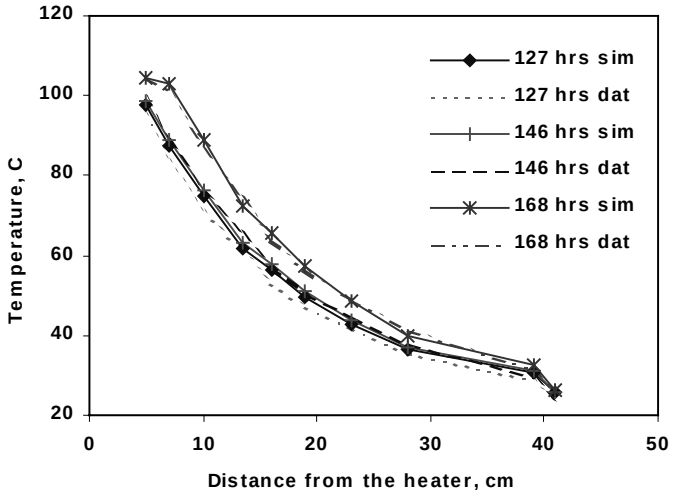

Figure 3.36 No Sensor 1 data: Temperature with respect to distance from heater.

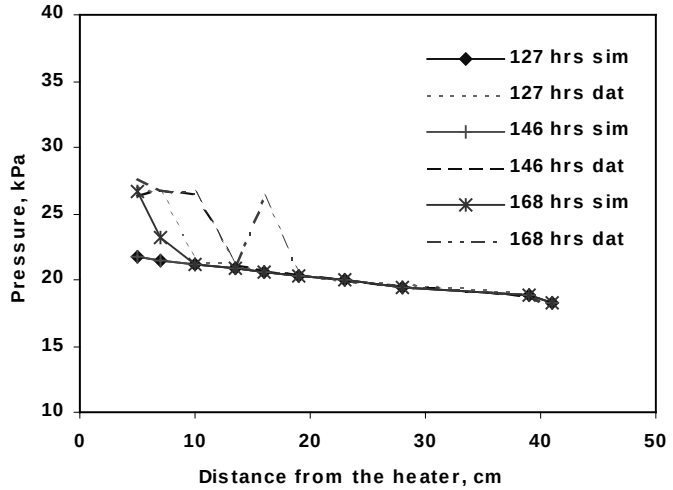

Figure 3.37 No Sensor 1 data: Pressure with respect to distance from heater.

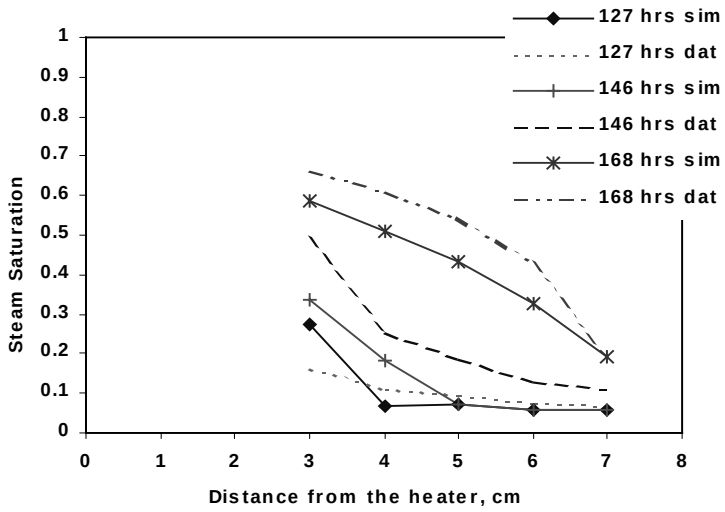

Figure 3.38 No Sensor 1 data: Steam saturation with respect to distance from heater.

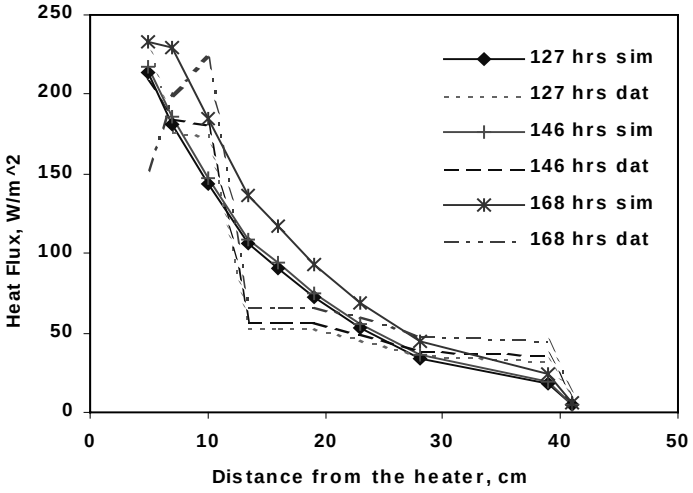

Figure 3.39 No Sensor 1 data: Heat flux with respect to distance from heater.

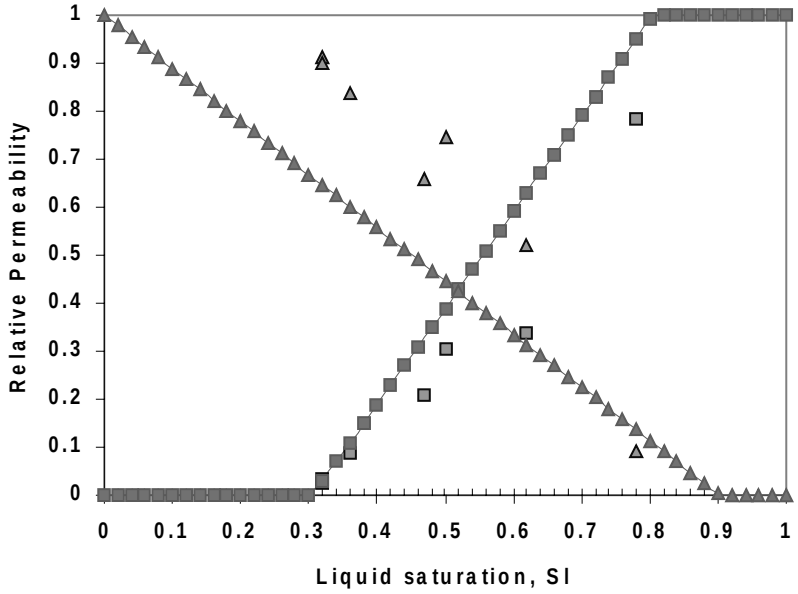

Figure 3.40 No Sensor 1 data: Relative permeability estimate compared with Ambusso's results (1996).

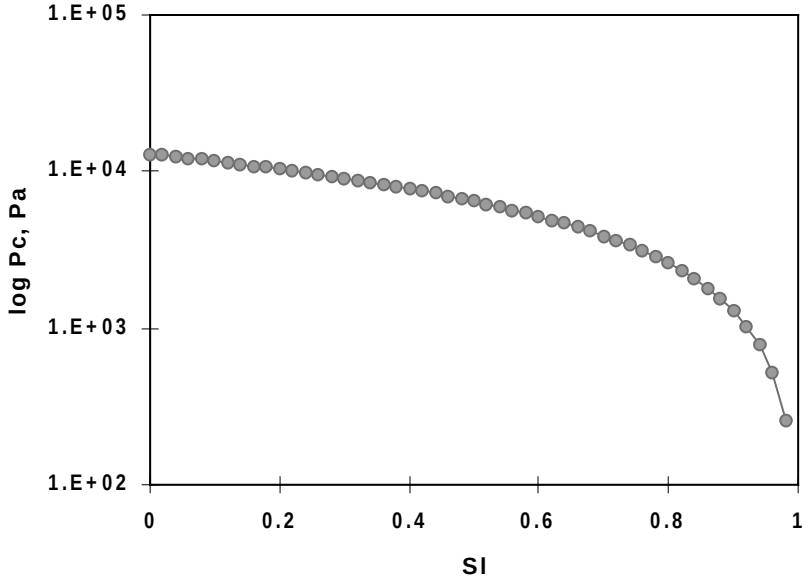

Figure 3.41 No Sensor 1 data: Linear capillary pressure.

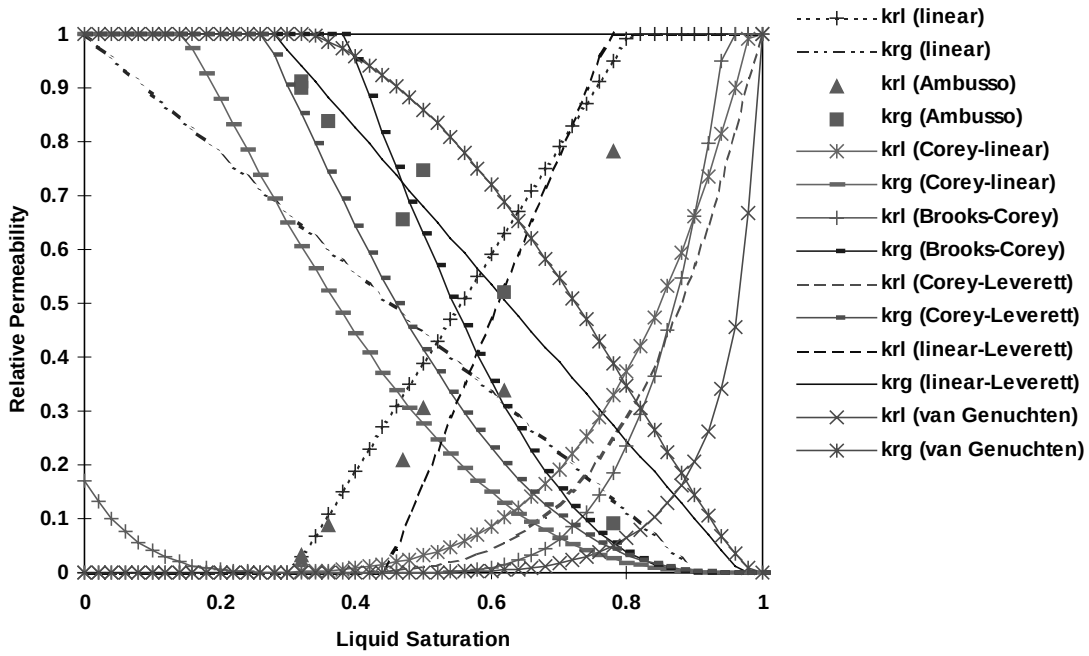

Figure 3.42 No Sensor 1 data: Relative permeability estimates compared with Ambusso's results.

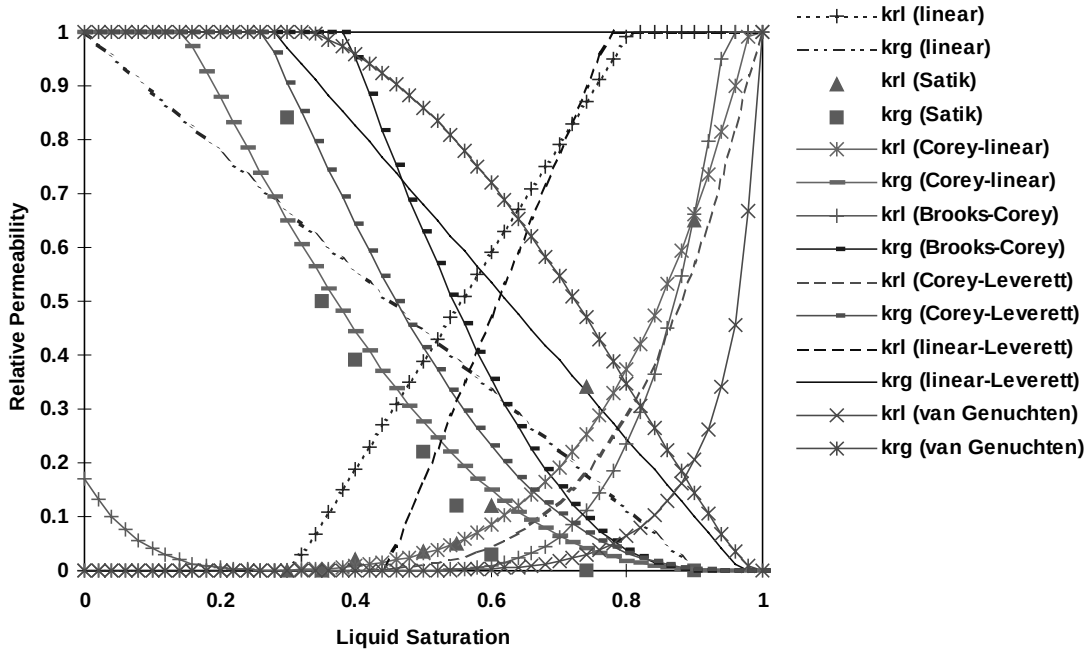

Figure 3.43 No Sensor 1 data: Relative permeability estimates compared with Satik's results.

3.6 CONCLUSION

1) Thermal and multiphase flow properties of a Berea sandstone core were estimated by inverse calculation using temperature, pressure, steam saturation, and heat flux data. The development of the two-phase flow region was strongly related to the temperature conditions in the core since heat was the only driving force in the experiment. As a result, the heat input as well as the thermal properties of the sandstone and insulation materials played a major role in understanding the system behavior. In addition, the high sensitivity of the insulation materials to the observation data and their strong correlation with the other parameters of interest made it difficult to obtain accurate estimates.
2) Although the linear relative permeability model gave the best fit in the two cases presented in the paper, all models yielded similar matches. This indicated that the data did not contain sufficient information to distinguish the different models, making the solution non-unique. Nonetheless, almost all models gave a consistent estimate for S_{gr}, which was around 0.1-0.2.
3) The choice for the capillary pressure model depended on the condition in the core, whether there was single-phase steam or two phases present. Since the distribution of steam depended heavily on the capillary pressure, the relative permeability would have been more accurately estimated had the capillary pressure been known.
4) The comprehensive analysis of all available data from a transient non-isothermal two-phase flow experiment provided an insight into the relation of processes and correlation of parameters. This information will be useful in the design of future experiments.

4. APPLICATION OF X-RAY CAT SCAN IN POROSITY AND SATURATION MEASUREMENT

This project is being conducted by Research Assistant Meiqing He, Dr. Cengiz Satik and Professor Roland Horne. The aim is to identify and to characterize fractures in geothermal rocks using X-ray computer tomography (CT). The porosity and saturation calculation processes are closely related to fracture calibration. In earlier reports, we discussed the fundamental physics of the CT technique and proposed two approaches for porosity and saturation calculation. For fracture interpretation, we proposed a denoising method, soft-thresholding the coefficients of wavelet transform, as a preprocess prior to edge detection in CT images. We applied the edge detection algorithm to CT images of Geysers core. In the last report we presented the Hough transform as a method to detect the line features in core CT images and the Active Contour Model for finding the connected contour of the fractures. In this report we applied these techniques to a sample of Geysers core. A general procedure of determining fracture aperture is proposed.

4.1 RESULTS

The procedures for edge detection, the Hough transform and the Active Contour Model were described in the previous quarterly report. In the current quarter we applied the Active Contour Model to a CT image of a Geysers rock sample. Figure 4.1 shows the contours of all the detected fractures.

After we have found the contours of the fracture, we can calculate the fracture aperture based on the calibration curve shown in Figure 4.2. Figure 4.3 shows an example of this approach, as applied to one of the identified fractures in Figure 4.1. Since the orientation of the contour shown in Figure 4.3 does not change much, we used the global Hough transform to estimate the orientation of the fracture and determine the appropriate location of the perpendicular profile. The orientation of the contour can be described by θ of 1.0472. (See the previous quarterly report for the definition of θ.) At the location shown in Figure 4.3(b) the aperture is 0.1226mm.

Natural fractures usually have changing orientation and aperture (see Figure 4.1). The procedure used to calculate aperture shown in Figure 4.3 may not be applied in such cases. To account for the variation of aperture, we calculated the aperture at each pixel on each contour of the fractures in the entire slice of the sample of Geysers core. Figure 4.4 shows the distribution of fracture aperture in Geysers sample. Most apertures are below 250 micron.

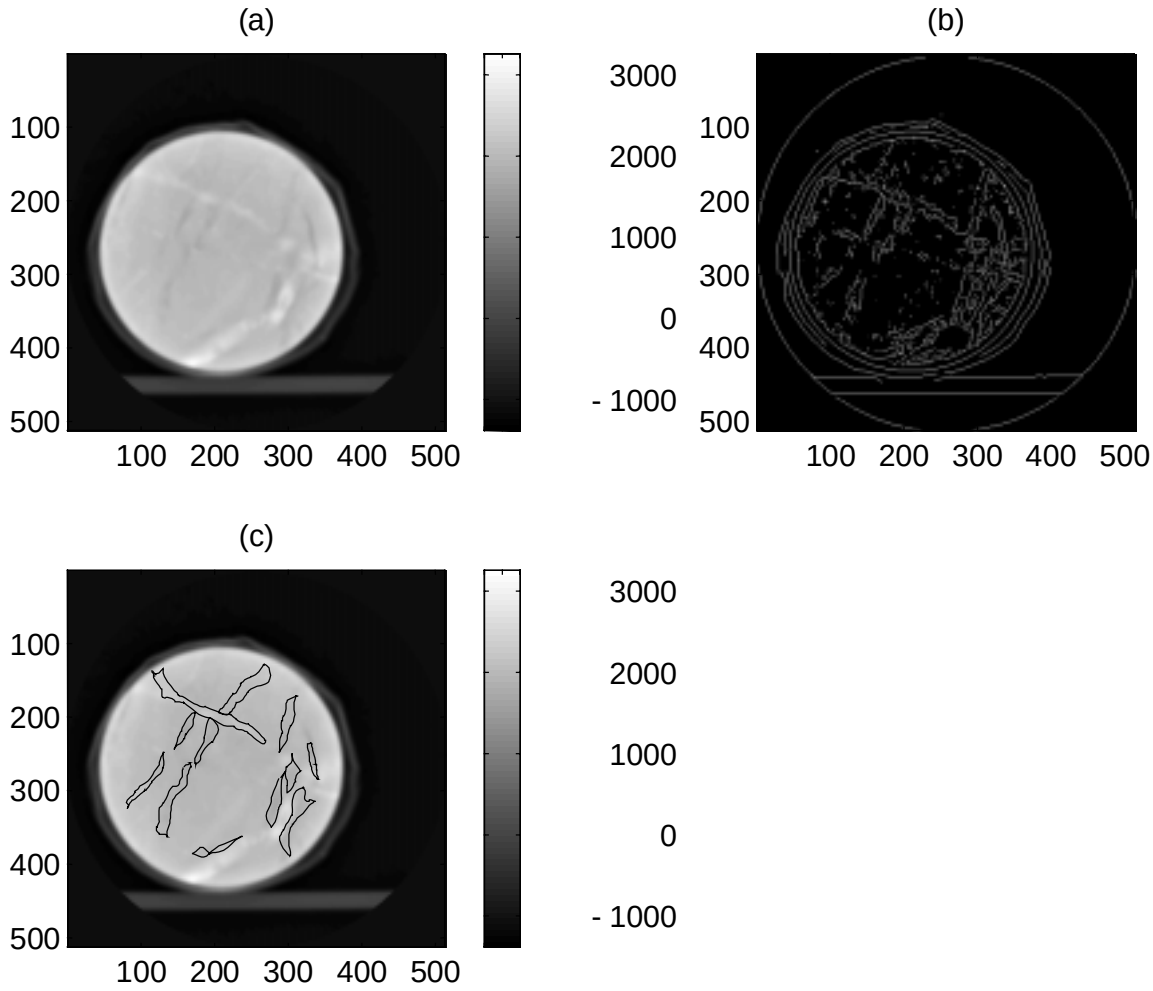

Figure 4.1:Finding fracture contours using snake (a) Original core image. (b) Edge map using Sobel gradient operator (thr=20) on the original image. (c) Connected contours found by snake.}

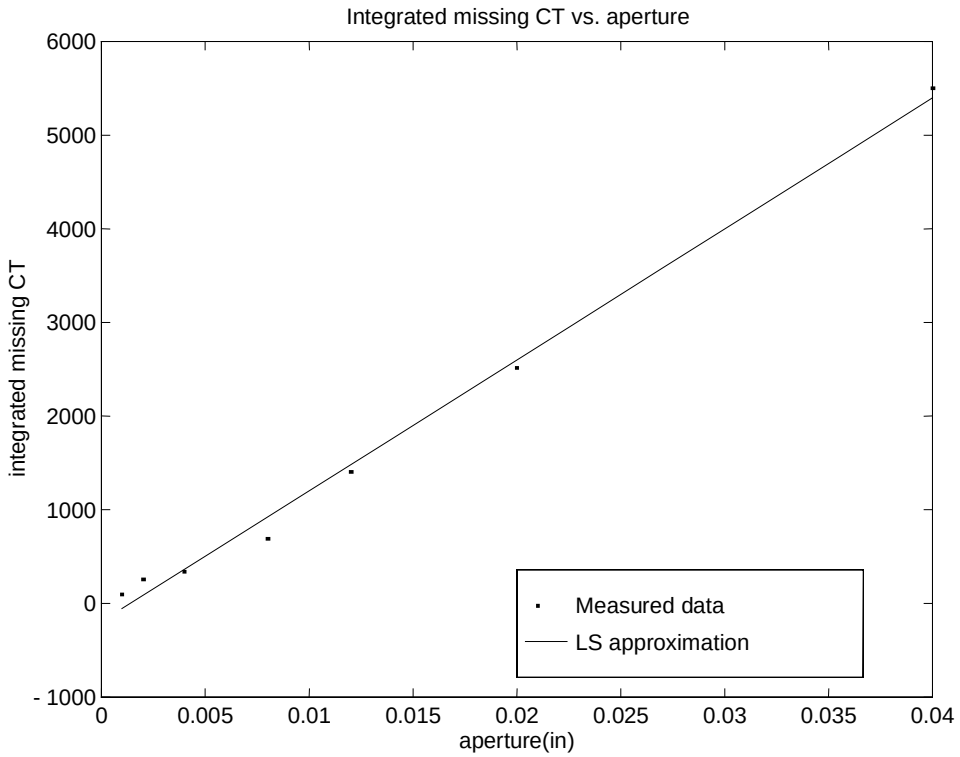

*Figure 4.2: Relationship between integrated missing CT and aperture: y=1.398e5*x-194.5402*

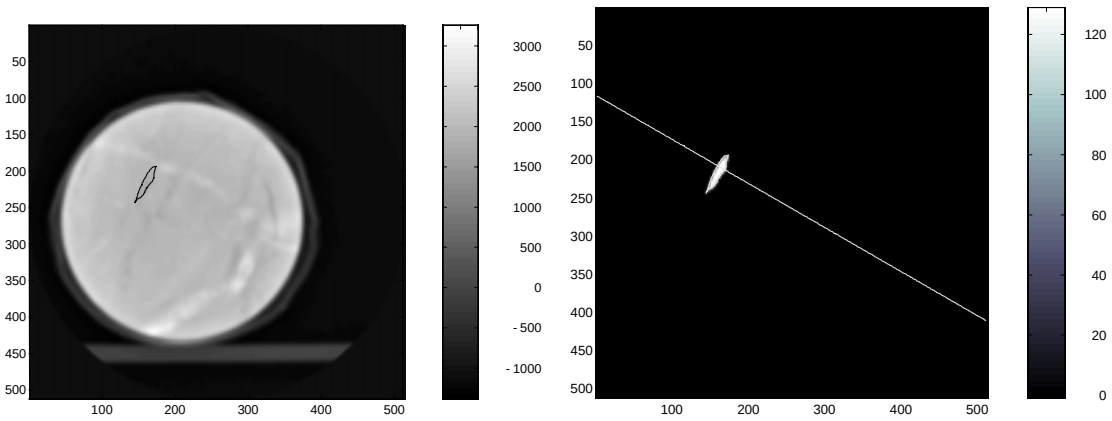

Figure 4.3: (a) Contour of a typical fracture in Geysers core. (b) Aperture calculation on the contour shown in (a).

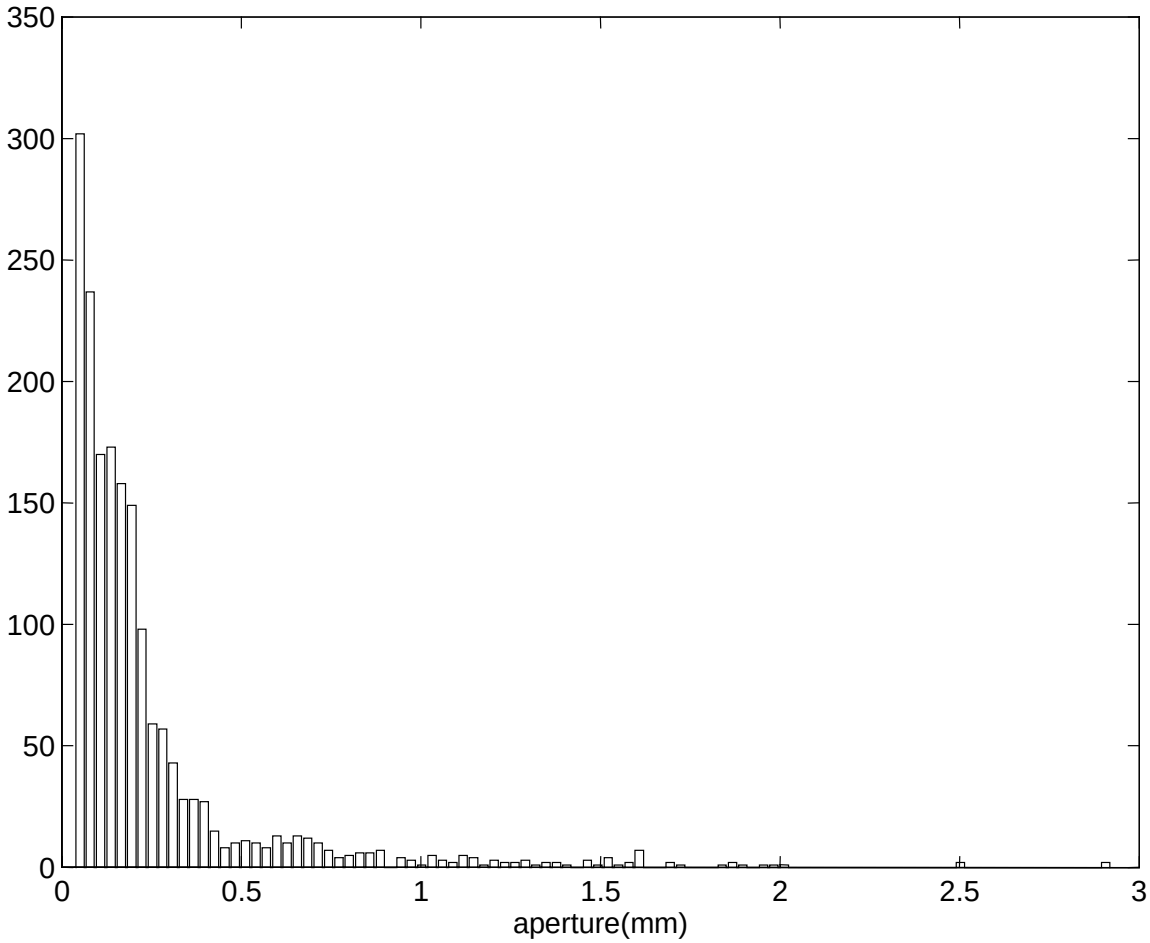

Figure 4.4 Aperture distribution in Geysers sample

4.2 CONCLUSIONS AND DISCUSSIONS

A general procedure for determining fracture aperture in geothermal rocks has been developed. The procedure includes the following steps:

(1) The experimental calibration of a curve of integrated missing mass vs. aperture using homogeneous material having similar density to the natural fractured core.

(2) Edge detection on the natural fractured core. A denoising procedure may be applied prior to edge detection.

(3) The active contour algorithm is used to refine the edge map.

(4) Components are labeled if necessary. This procedure is useful when we need to address an individual contour in an image.

(5) The identified fracture orientation is estimated using the Hough transform. The fracture aperture size is inferred from the empirical curve of integrated missing CT number vs. fracture aperture obtained from the calibration experiment. The saturation of fluid in the fracture region can also be estimated.

For the detection of a regular fracture, we can use the global Hough transform to estimate the orientation of the fracture. For a natural fracture, we can use the local Hough transform. The window of the local transform is adjustable according to the variation of the fracture orientation.

In our application of the snake model, the initial curve is placed outside of the object of interest, and internal forces guide the snake to find its way. Spurious points inside the desired contour do not have any influence on the contour obtained. This way of setting the initial contour is easier than the one presented by Cohen(1990). However, if there is a nearby object that is too close to the object of interest, the initial curve has to be placed closer to the one under study.

The denoising procedure is only necessary when the edge map is too noisy. The Active Contour method has resistance to noise while finding the contour.

One of the advantages of the snake model that can be explored in the future is the flexibility of including constraints, such as edge information. We can utilize the previous achievement in edge detection, for instance the Canny-Deriche edge detector (Canny, 1986) and edge detection using the wavelet transform. The attraction forces can be defined by simulating a potential obtained by convolving the binary edge image with a Gaussian impulse response. This can attract the snake to the small edge segments.

In general, the Active Contour model combined with the edge detection and Hough transform can significantly improve the detection quality of closed fractures, while enhancing the computational stability and reducing the complexity. Making use of edge detection, the Hough transform and the Active Contour model, we were able to characterize the fracture aperture distribution in a sample core from the Geysers geothermal field.

This project concluded during the current quarter. A technical report on this work has been prepared.

5. PROPAGATION OF A BOILING FRONT IN A FRACTURE

This project is being conducted by Research Assistant Robert DuTeaux, and Professor Roland Horne. The goal of this study is to analyze the propagation of thermal front with boiling flow in a fracture. Research continued this past quarter with the intent of modeling fluid flow and heat transfer in low matrix permeability fractured reservoirs.

5.1 INTRODUCTION

The observation of experimental phenomena has led to a better understanding of the coupling between fluid flowing in a fracture and heat transfer from the matrix. Because fluid flow and heat flux at a fracture surface are so highly coupled, carefully modeling the flow in a fracture is necessary for accurately modeling boiling heat transfer in a fracture. Multiphase flow in a fracture is not well understood, however, and the interaction of viscous, gravity, and capillary forces in large fractures may not be precisely described by existing relative permeability functions. A review of literature on fractured flow indicates that the role of capillary pressure in a fracture has been controversial. Also, an analysis of characteristic dimensional scales has been important for understanding the transport of heat and fluid in fractured systems. These issues are discussed, and preparations for experimental work are described in this report.

Initially, this research began with the goal of describing the thermal front associated with injection into and boiling in a fracture. At that time the difficulties of describing multiphase flow in a rock fracture with a relatively impermeable matrix were not fully realized. The significant roles of fracture spacing and the velocity of flow, however, were recognized, and the propagation of a thermal front was intended to be described in terms of these parameters. During the course of this research a strategy for modeling the thermal front by quantifying a boiling convection coefficient has emerged, but the hydraulic nature of multiphase flow through fractures and influence of a porous surface with boiling required further research. For these reasons a second experimental apparatus was built. Because this investigation needs to be concluded by the end of the summer quarter, the spring quarter was taken as an opportunity to analyze the essential elements of multiphase flow and heat transport in fractured media. A brief description of experimental preparations and a discussion of the difficulties with relative permeability and thermal energy transport follow.

5.2 EXPERIMENTAL PREPARATIONS

The plan for a systematic set of experiments, with both the transient and the steady state experimental apparatuses, has been made over the past quarter. (Please see the previous quarterly report for further explanation of these experiments.) Illustrations of the transient and steady state apparatuses are shown in Figure 5.2.

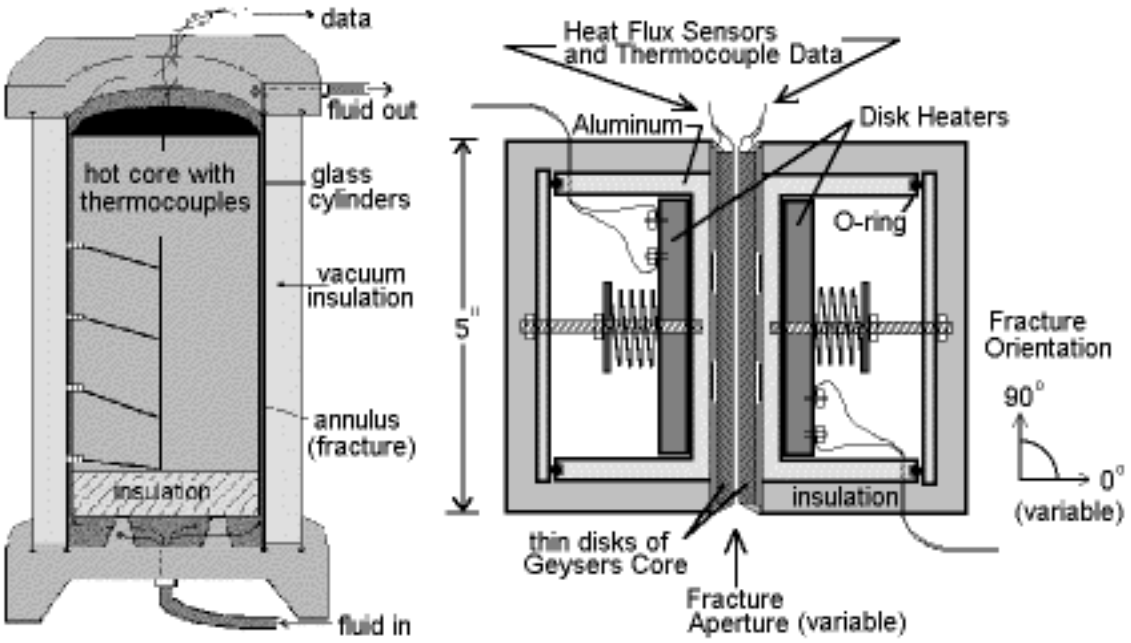

Figure 5.2: Transient experiment, Steady state experiment.

In the transient experiment, the use of shrink fit Teflon to hold thermocouples in place was abandoned because it decreased the wettability of the surface and caused constrictions and uneven flow through the annulus of the concentric glass cylinders. Instead, the glass surface was sandblasted and thermocouples have been attached with small drops of high temperature epoxy. A set of boiling experiments at various flow rates has been planned and will be conducted over the summer quarter. In a manner similar to that described in the previous quarterly report, heat flux will be plotted with respect to glass surface temperature in order to quantify a boiling convection coefficient.

The steady state boiling apparatus has been modified by adding an aluminum disk between the opposing rock surfaces that form a simulated fracture. (This is not shown in Figure 5.2) The aluminum disk has a fluid port on its side and an opening at its center, to allow forced radial flow across the rock (Geysers core) surfaces. Thus, in addition to controlling aperture, orientation, and the heat flux to the rock surfaces, the influence of forced injection (or production) of flow will be investigated. Furthermore, an additional thin disk of rock for each side of the apparatus has been prepared for thermocouples to be placed midway between the heater and the fluid surface. This was necessary to better capture the shape of the temperature gradient to the porous surfaces since preliminary experiments showed that boiling occurred inside the rock and tiny vapor bubbles were exiting at the surface. A systematic investigation of a boiling heat transfer coefficient will be conducted this summer, with the hope that flow and boiling regimes can be investigated by varying fracture aperture, fracture orientation with respect to gravity, and flow velocity.

5.3 DISCUSSION OF RESEARCH

Geothermal reservoirs are often modeled as porous media with a continuum formulation of the conservation of mass, energy, and momentum over a representative elemental volume (REV). While these balances are valid physical constraints, unfortunately, they do not guarantee a simulation is based upon the physical aspects of fluid flow and heat transport in an actual reservoir. Relative permeability has been a fundamental tool for upscaling pore level multiphase flow, however, the validity of relative permeability becomes uncertain for describing the flow of steam and water in a fractured reservoir. Also, because the transport of fluid and heat often operate on vastly different characteristic time scales, simulation incompatibilities arise when attempting to model these behaviors simultaneously.

If the difficulty of describing multiphase flow in a fracture can be overcome, and if a convection boiling coefficient can be quantified, then fluid flow and heat diffusion in the matrix can be modeled on their own characteristic time scales and coupled by a convection coefficient. This would potentially become more useful than porous continuum models for describing the propagation of a thermal front in a fractured reservoir. While this is generally the idea of a dual porosity model, it has been useful to re-examine the fundamentals of a REV and question the utility of describing multiphase flow by relative permeability functions.

5.3.1 Representative Elemental Volume (REV)

The idea of a REV is fundamental to the derivation of the continuity of mass, momentum, and energy equations in a continuum model. This volume defines a characteristic dimensional scale for the discretization of a simulation model. On the REV scale, reservoir quantities are considered uniformly distributed. That is, any larger volume would have the same properties, but smaller volumes would not necessarily represent reservoir quantities on a simulation scale. Thus, the standard formulation of a continuum assumes homogeneous porosity, permeability, phase saturations, and temperature within a REV. Thermodynamic equilibrium within a REV is also commonly assumed. The unavoidable problem in modeling a fractured reservoir as a continuum is that the REV must be larger than the spacing of major permeable fractures. Since some geothermal reservoirs have large scale fault controlled permeability (for example, Beowawe Nevada, Faulder 1997), this implies that a REV could be larger than the injection-production well spacing.

5.3.2 Relative Permeability

Because heat is transported primarily by convective flow, the flow model of a geothermal reservoir has a large influence on its thermal behavior. Properly characterizing the hydraulic nature of flow in a fractured reservoir is vital to the analysis of a thermal front associated with injected water. Therefore, the physical basis of steam-water relative permeability has been examined.

Relative permeability functions initially assume a locally uniform vertical saturation distribution (Dake 1978). In a fracture this assumption is easily challenged if the fracture aperture is large enough to allow segregation of phases.

Capillary pressure curves represent the relative immobility of wetting and nonwetting (assumed immiscible) phases in a pore space as a function of the degree of phase saturation. In small fractures and porous rocks with a non-negligible capillary pressure, a pore size distribution leads to a distribution of phases segregated into the larger and smaller pores of a rock. Capillary forces therefore relate relative permeability to saturation, since (ideally) the degree of saturation determines the sizes of pores available for the flow of each phase. In larger fractures, where capillary pressure has less influence, these concepts become controversial. For example, in most fractured reservoir simulations capillary pressures in fractures are set to zero (Chen J. 1991, Chen W. 1987, Kazemi 1979 1992). Others argue that capillary pressure in a fracture should not be zero (Firoozabadi 1990, Labastie 1990). The reality lies in the fact that capillary pressure is a function of pore size (and interfacial tension), so the aperture dimension (and temperature) of a fracture determines the magnitude of capillary forces. In a sufficiently large fracture, however, the relative magnitude of capillary forces compared to viscous and buoyancy forces should be considered.

The appropriateness of steam-water relative permeability in either porous or fractured rock can also be viewed with skepticism in other respects. For steam and water, mass transfer across the phase interface is not only possible, it is a mechanism of energy transport. Boiling and condensation phase transitions in pores are also possible, therefore the dimensions of pores (large or small) that either phase occupies will depend upon thermodynamic conditions (Udell 1982). When boiling occurs, the pore size occupied by either steam or liquid is ill-defined because nucleate boiling suggests vapor could originate in the small pores. This contradicts the concept that the non-wetting phase occupies only the larger pores. These arguments suggest that steam-water multiphase flow is more complex than relative permeability functions usually assume, and scrutiny of the physical basis of conventionally defined relative permeabilities is merited.

Because capillary forces decline and allow viscous and buoyancy forces to prevail as the dimension of a fracture aperture increases, a consideration for the relative magnitudes of forces on the fluid has been determined to be physically meaningful. In sufficiently large fractures, gravity segregation of steam and liquid water may result. In the absence of gravity, the relative permeabilities of segregated phases simply become proportional to the fractions of concurrently flowing phases. This leads to the familiar X-curve relative permeabilities used in geothermal simulation (for lack of a better model). However, with large flow velocities (high capillary number conditions), and buoyancy forces applied to the fluid, relative permeability becomes a function of the ratios of capillary, viscous, and buoyancy forces. In a vertical fracture, for example, the presence of vapor assists the upward flow of liquid and retards its downward flow. Momentum exchange between

flowing phases is possible. This was confirmed by the videotape of transient experiments where instability and cyclic flow of liquid was observed as liquid and vapor exchanged momentum. Therefore, conventional relative permeability functions appear to ignore some of the important physical mechanics when describing multiphase flow in fractured geothermal reservoirs.

5.3.3 Thermal Energy Transport

In a fractured reservoir, thermal energy is transported by convection with flow in fractures, and moves by both conduction and convection in the matrix. Conduction in the matrix is driven by a temperature gradient, and fluid convection is driven by a pressure gradient. In a low permeability fractured reservoir, convective thermal energy transport can be rapid along major fractures, and many orders of magnitude slower in the matrix.

Heat flux in the rock matrix is proportional to thermal conductivity, and the velocity of fluid flow in the matrix. In typical geothermal rocks in fractured reservoirs, both of these quantities are relatively small. Since conductivity is small, thermal diffusivity (which is the ratio thermal conductivity / volumetric heat capacity) is also relatively small. The thermal diffusivity of rock describes and couples the characteristic time and length dimensional scales for conductive heat diffusion. Many rocks, including Geysers rocks, have thermal diffusivities on the order of 1.0 E -6 m^2/s. This characterizes the time scale for heat diffusion because the distance heat energy travels is proportional to the square root of the thermal diffusivity - time product.

$$L_c = \sqrt{(\alpha\, t)} \quad \text{or similarly,} \quad t_c = L^2 / \alpha \qquad \alpha = \text{thermal diffusivity}$$

This means that a temperature perturbation travels at a speed (on the order) of one millimeter [$\sqrt{}$ (1.0 E -6 m^2/s)* (1 s)] in one second. This also means that the quantity of thermal energy than can be transported by conduction from the matrix is very limited by such small thermal diffusivity. The quantity of energy delivered to the flow in a fracture is, therefore, controlled by the thermal diffusivity of the matrix. Since the injected water, (with its large heat capacity), moves relatively quickly through a fracture, only a relatively small quantity of energy conducts to the fluid. Therefore, fluid proceeds along a fracture without being heated to the temperature of the nearby rock, just a few meters away.

For illustration, since there are about 31 million seconds in one year, a temperature perturbation diffuses across 5.6 meters of rock in one year, across 17.7 meters in 10 years, and across about 31 meters of rock in 30 years, which is much smaller than a typical grid block in a field scale simulation. Heat diffusion, therefore, operates on a much smaller characteristic length scale (and much larger time scale) than heat convection in major fractures, and thermal equilibrium can not be assumed on large scales. Early thermal breakthrough occurs because the time scale for injected fluid to reach the production well is not balanced to the time scale of thermal diffusion across the distance between

fractures. In fact, for widely spaces fractures, the characteristic time scales may differ by five orders of magnitude or more.

5.4 FUTURE WORK

With the considerations previously discussed, it has seemed prudent to quantify a boiling convection coefficient experimentally and work toward building a model that simulates energy transport by diffusion in a rock matrix, and couples this with convective transport along a fracture. This would provide a potential for modeling fractured geothermal reservoirs with treatment of heat and fluid transport on appropriate dimensional scales, albeit this requires significant further research. Investigating the hydraulic nature of multiphase flow in fractures, and measuring the heat flux to the surface of a fracture during boiling are the major objectives of the experiments to be conducted this summer.

6. MODELING OF GEOTHERMAL RESERVOIRS CONSTRAINED TO INJECTION RETURN DATA

This project is being conducted by Research Assistant Ma. Michelle Sullera and Prof. Roland Horne. It aims to deduce injection return mechanism(s) and flow paths from correlations between producer chloride concentration and injection operating parameters (flow rate and injection chloride). The project was completed during the current quarter, and a technical report on the results was issued.

6.1 BACKGROUND

Previously, it was proposed that chloride and injection data be decomposed into *detail* and *approximation* wavelet functions; and, that the resulting *detail* functions be subjected to regression analysis. The choice of modeling *details* over *approximations* was based on the fact that the effect of changes in injection rates is expected to manifest as short-term variations in reservoir chloride concentrations and detail functions represent these short term fluctuations.

Because the approximation functions isolate and retain the general trend in chloride with time, multiple regression of the details does not require a time term in the linear model. Thus, we used the following model:

$$Cl_p = a_1 Q_{I1} + a_2 Q_{I2} + a_3 Q_{I3} + \ldots \quad \ldots + a_n Q_{In} \qquad (6.1)$$

where Cl_p = chloride concentration detail in production well, P

Q_{In} = injection rate detail in injection well I_n

a_n = linear coefficient of well I_n

Comparison of coefficients obtained by using model (6.1) allows us to differentiate the degree of connectivity of different injectors to a given producer. Since details are deviations from local averages multiple regression using details ignores the differences in base chloride levels between producers. Regression results for different producers may therefore be intercorrelated; more specifically, the coefficients obtained may be used to compare the contributions of an injector to different production wells and consequently, to verify any conclusions drawn from the analysis against tracer test results.

Regression was done for levels 1, 2, and 3 of the detail functions of Palinpinon-I chloride and injection data set. The following sections compare the results of the regression analysis with tracer test data and qualitative field observations.

6.2 COMPARING RESULTS OF REGRESSION ANALYSIS OF DETAIL WAVELET FUNCTIONS WITH TRACER TEST DATA

Two sets of radioactive tracer test results were available for comparison with results of our analysis: that of the test conducted on well PN-9RD and one on OK-12RD. Both sets were reported by Macario (1991) and are reproduced in Table 6.1. Macario (1991) defined mean transit time as the time it takes for half of the tracer return to reach the

production well. Assuming that the mean transit time measures the degree of connectivity between the injector tested and a producer (lower transit times corresponding to stronger connections) Table 6.1 lists the production wells in order of *decreasing* connectivity with the injector. Correspondingly, Tables 6.2 and 6.3 lists the wells affected by OK-12RD and PN-9RD, respectively, in the order of decreasing coefficients based on regression on all three detail levels.

Table 6.3 shows, with the exception of one well, that all wells affected by PN-9RD had positive coefficients. Comparison of Table 6.3 with Table 6.1 shows that tracer return was indeed monitored in all wells shown by regression analysis to be affected by well PN-9RD, including PN-29D which had a negative coefficient. More importantly it shows that the order of the strength of connection between PN-9RD and the wells monitored in the tracer test was most closely mimicked by the results of regression on detail level 3 with OK-7D showing the strongest connection to PN-9RD and PN-29D, PN-16D, and PN-23D displaying connections of about the same strength.

Monitored Well*	Mean Transit Time, days
PN-9RD Tracer Test	
OK-7	5.4
PN-26	13
PN-28	14
PN-29D	15.4
PN-30D	15.7
PN-23	15.8
PN-16D	16
PN-19D	16
PN-31D	16
PN-18D	17.2
OK-9D	monitored, no return
OK-12RD Tracer Test	
PN-15D	7.3
OK-10D	13.8
OK-7D	14.6
PN-29D	monitored, no return

** Only wells which have chloride data are reported here.*

Table 6.1 Radioactive tracer test results for PN-9RD and OK-12RD.

OK-12RD

Affected Well	Coefficient
d1	
OK-10D	12.38
d2	
PN-23D	2.46
PN-29D	-4.05
PN-31D	-10.82
d3	
PN-15D	125.27
PN-16D	-7.40
PN-29D	-3.34
PN-30D	6.15

Table 6.2 Regression results for OK-12RD.

PN-9RD

Affected Well	Coefficient
d1	
PN-30D	5.74
PN-29D	3.99
PN-16D	1.47
d2	
PN-19D	4.87
PN-18D	4.06
OK-7D	2.96
PN-16D	2.02
PN-29D	-11.65
d3	
OK-7D	9.40
PN-29D	1.83
PN-16D	0.92
PN-23D	0.43

Table 6.3 Regression results for PN-9RD.

On the other hand, comparison of Table 6.2 with Table 6.1 shows that tracer return was observed in two of the seven wells shown by regression analysis to be affected by well OK-12RD. Four of the seven wells were not monitored during the tracer test. As with PN-9RD, the well which is most connected to OK-12RD based on the tracer test had the highest coefficient at level 3 regression.

Based on these observations we have concluded that regression analysis of details at level 3 best assesses the degree of connectivity between wells: high positive coefficients correspond to strong connections and, negative and low positive coefficients correspond to weak connections.

6.3 CHECKING REGRESSION RESULTS AGAINST QUALITATIVE FIELD OBSERVATIONS

Harper and Jordan (1985) reported the following observation: from May 1984 to October 1984 a large increase in reservoir chloride occurred in production wells PN-19D, 23D, 29D, 31D, OK-7D and OK-9D when reinjection was shifted to the wells PN-7RD and PN-8RD. This observation matches the results of level 3 detail analysis for well PN-8RD as outlined in Table 6.4: OK-7D, PN-19D, and PN-31D were all found to be strongly connected with PN-8RD. PN-23D, -29D, and OK-9D may have been receiving reinjection returns from OK-7D but no injection rate data from OK-7D was available to allow verification with regression results.

PN-8RD

Affected Well	Coefficient
d3	
OK-7D	3.14
PN-16D	0.64
PN-18D	2.76
PN-19D	4.93
PN-30D	-1.36
PN-31D	10.49

Table 6.4 Level 3 regression results for PN-8RD.

On the other hand, Amistoso and Orizonte (1997) reported that OK-10D and PN-20D experienced enhanced steam flows and they attributed it to reinjection fluids intruding into the production sector at deeper levels. They cited the wells TC-2RD, TC-4RD, PN-3RD and PN-5RD to be wells which are providing pressure support to the reservoir due to deep injection but attributed the enhanced steam flow in OK-10D and PN-20D to TC-2RD and TC-4RD, specifically. Regression analysis results for these wells (Table 6.5), however, show that OK-10D is not affected by TC-2RD; rather it is affected by PN-1RD, PN-2RD, and PN-3RD between 1986 and 1990 and by PN-3RD, TC-3R, N3 and OK-3R between 1990 and 1996. It is worth noting that the effect of PN-3RD on OK-10D was found to be consistent between the intervals 1986-1990 and 1990-1996 as reflected by close *r* values for the two periods (-0.79 and -0.77). The large positive coefficient of well N3 is suspect however as it conflicts with its negative *r* value. PN-20D was also analyzed to be affected by PN-3RD. The effect of TC-2RD and TC-4RD on PN-20D could not be ascertained from regression analysis due to insufficient chloride data from PN-20D after 1990.

Pamatian (1997) reported that reinjection fluid from TC-2RD neutralized the fluid acidity in wells OK-10D and PN-13D. Again, the effect of TC-2RD on OK-10D was not substantiated by regression results but its effect on PN-13D was (Table 6.6). Again, terms with conflicting *r* and coefficient signs posed interpretation problems.

OK-10D (1986-1990)

d3

Regression Statistics	
Multiple R	0.839369312
R Square	0.704540842
Standard Error	79.20406691
Observations	48

	Coefficients	*r (simple)*	*Standard Error*	*t Stat*	*P-value*
pn1rd	1.0860989	0.742898166	0.432894148	2.508924886	0.01577982
pn2rd	-3.71087522	-0.72596153	1.775342121	-2.09023105	0.04227759
pn3rd	-4.4114713	-0.78948113	1.783793986	-2.4730834	0.01723762

OK-10D (1990-1996)

d3

Regression Statistics	
Multiple R	0.835160095
R Square	0.697492385
Standard Error	150.1670809
Observations	80

	Coefficients	*r (simple)*	*Standard Error*	*t Stat*	*P-value*
pn3rd	-11.4979076	-0.77103302	1.485833395	-7.7383559	3.4832E-11
tc3r	1.704839524	0.522611064	0.404330736	4.216448003	6.7759E-05
n3	30.87773863	-0.65393407	6.498963063	4.751179278	9.3559E-06
ok3r	-7.36184797	-0.36088849	2.134566707	-3.44887229	0.00092135

PN-20D (1983-1989)*

d3

Regression Statistics	
Multiple R	0.635764265
R Square	0.404196201
Standard Error	495.2038572
Observations	80

	Coefficients	*r (simple)*	*Standard Error*	*t Stat*	*P-value*
pn1rd	10.21445053	0.346132276	1.741845857	5.864152953	1.0654E-07
pn3rd	12.28448348	0.357197703	2.153358367	5.704802167	2.062E-07
pn6rd	4.493768629	0.105136293	1.637086662	2.744979074	0.00752785

**No chloride data was available from 1990 to 1993 and remaining data points were not sufficient for analysis.*

Table 6.5 Level 3 regression statistics for OK-10D and PN-20D.

PN-13D (1990-1996)

d3

Regression Statistics	
Multiple R	0.962568329
R Square	0.926537788
Standard Error	74.57273176
Observations	70

	Coefficients	*r (simple)*	*Standard Error*	*t Stat*	*P-value*
tc2rd	4.826890146	0.403207897	0.459363951	10.5077687	1.4452E-15
tc3r	1.989170863	0.37912479	0.16882133	11.78269865	1.1114E-17
tc4r	52.80156771	-0.47305009	4.657792303	11.33617909	5.9844E-17
ml1rd	-191.386684	-0.73129226	16.95558741	-11.2875289	7.1995E-17
n3	11.67741779	-0.76944945	1.849731659	6.313033424	2.9328E-08
ok3r	27.49754181	-0.47241942	2.227450499	12.34484978	1.3816E-18

Table 6.6 Level 3 regression statistics for PN-13D.

6.4 CONCLUSIONS AND RECOMMENDATIONS

Qualitative field observations and tracer test data agreed best with the results of regression on level 3 *detail* of chloride concentration and injection rates in Palinpinon-I: wells identified by tracer tests to be strongly connected had high positive coefficients and weak connections were indicated by negative and low positive coefficients at level 3 regression. This suggests that producer-injector interactions are best detected by correlating changes in chloride concentration over periods of four months (corresponding to level 3 resolution) with corresponding four-month fluctuations in injection rates. While the good correlation at such a relatively low level of time resolution may be explained as the result of the natural dispersion of chloride and injection rate signals as they propagate through the reservoir, it is also possible that this is due to the loss of information brought about by the use of monthly averaged data values in the analysis. It is therefore recommended that both chloride and injection rate data be recorded more frequently and the analysis be done on this larger data set. It is also possible that the Haar wavelet that was used in signal decomposition was too coarse in that it contributed to the loss of texture in the data. Investigation of the effects of using smoother wavelets is also recommended.

Emphasis is also placed on the need for continuous data measurements when doing wavelet analysis. Highly intermittent measurements result in data loss: since it is considered safe to interpolate only over short periods of time, the lack of data over long time intervals forces one to disregard the data collected prior to such periods when doing the analysis.

Another possible improvement to consider in future regression analyses is to take into account possible nonlinearity in the variation of chloride with injection rates. While nonlinearity does not invalidate the analysis, it certainly weakens it as the relationship between chloride concentration and injection rates is not completely captured by the

coefficients of the linear model. Although regression analysis uses a linear model, effects of nonlinearity in the variation of chloride with injection rates may be incorporated into the model by using nonlinear terms: the model is kept linear even though the individual terms are not. Results of this modified analysis will be more difficult to interpret however, because the strength of interaction between producers and injectors will be measured not only by the magnitude of the coefficients but also by the exponent of each term.

REFERENCES

Ambusso W.J., 1996. Experimental Determination of Steam-Water Relative Permeability Relations, MS Thesis, Stanford University, Stanford. Calif.

Amistoso, A.E. and Orizonte, R.G., Jr., 1997, "Reservoir Response to Full Load Operation Palinpinon Production Field Valencia, Negros Oriental, Philippines", Proceedings of 18th PNOC-EDC Geothermal Conference.

Brooks R.H. and Corey A.T., 1964. "Hydraulic Properties of Porous Media", Colorado State University, Hydro paper No.5.

Canny, J.: "A Computational Approach to Edge Detection", IEEE Transactions on Pattern Analysis and Machine Intelligence, November, 1986.

Chen J., Miller M.A., Sepehrnoori K. (1991). Comparisons of counter-current imbibition transfer functions in dual porosity models of naturally fractured reservoirs. In-Situ (1991):115-147.

Chen W.H., Wasserman M.L., Fitzmorris R.E. (1987). A thermal simulator for naturally fractures reservoirs. SPE Paper No. 16008. Presented at SPE Symposium of Reservoir Simulation, San Antonio, TX, Feb. 1-4, 1987.

Cohen, L.D. and Cohen, I.: "A Finite Element Method Applied to New Active Contour Models and 3D Reconstruction from Cross Sections." Proceedings 3rd International Conference on Computer Vision, Osaka, Japan, 1990.

Corey A.T., 1954. "The Interrelations Between Gas and Oil Relative Permeabilities", Producers Monthly Vol. 19 pp 38-41.

Corey A.T., 1994. *Mechanics of Immiscible Fluids in Porous Media*, Water Resources Publications.

Dake L.P., 1978. *Fundamentals of Petroleum Engineering*, Elsevier Science B. V.

Dullien F.A., 1992. *Porous Media Fluid Transport and Pore Structure*, Academic Press.

Faulder D.D., Johnson S.D., Benoit W.R. (1997). Flow and permeability structure of the Beowawe, Nevada hydrothermal system. Proc. 22nd Workshop on Geothermal Reservoir Engineering, Stanford University, Stanford, CA, Jan 27-29, 1997 (SGP-TR-155), 63-71.

Finsterle S., 1997. ITOUGH2 Command References Version 3.1, Lawrence Berkeley National Laboratory, Berkeley, Calif.

Finsterle S., Pruess K., Bullivant D.P., and O'Sullivan M.J., 1997. "Application of Inverse Modeling to Geothermal Reservoir Simulation", Proc. of 22rd Workshop on Geothermal Reservoir Engineering, Stanford, Calif.

Finsterle S., Satik C., and Guerrero M., 1998. "Analysis of Boiling Experiments Using Inverse Modeling, Proc. of 1st ITOUGH2 Workshop, Berkeley, California.

Firoozabadi A., Hauge J (1990). Capillary pressure in fractured porous media. J Petrol Tech (June 1990):784-791.

Garg S.K. and Pritchett J., 1977. "On Pressure-Work, Viscous Dissipation and Energy Balance Relation fro Geothermal Reservoirs, Advances in Water Resources, **1**, No. 1, 41-47.

Grant M.A., 1977. "Permeability Reduction Factors at Wairakei", Proc. of ASME/AIChe Heat Transfer Conference, Salt Lake City, Utah, 77-HT-52, 15-17.

Harper, R.T. and Jordan, O.T., 1985, "Geochemical Changes in Response to Production and Reinjection for Palinpinon-I Geothermal Field, Negros Oriental, Philippines", Proceedings of 7th New Zealand Geothermal Workshop.

Horne R.N. and Ramey, H.J. Jr., 1978. "Steam/Water Relative Permeabilities From Production Data", GRC Trans. (2), 291.

Johns, R.A.: "Diffusion and Dispersion of Solute in a Variable Aperture Fracture", 1991, Ph. D. dissertation, Stanford University.

Kass, M., Witkin, A. and Terzopoulos, D.: "Snake: Active Contour Models", International Journal of Computer Vision, 1987.

Kaviany N., 1995. Principles of Heat Transfer in Porous Media, Mechanical Engineering Series, Springer.

Kazemi H., Merrill L.S. (1979). Numerical simulation of water imbibition in fractured cores. Soc. Petrol. Eng. J. (June 1979):175-182.

Kazemi H., Gilman J.R., Elsharkawy A.M. (1992). Analytical and numerical solution of oil recovery from fractured reservoirs with empirical transfer functions. SPE Res Eng (May 1992):219-227.

Labastie A. (1990). Capillary continuity between blocks of a fractured reservoir. SPE Paper No. 20515. Presented at the 1990 SPE Annual Technical Conference and Exhibition, New Orleans, LA, Sept 23-26, 1990.

Leverett M.C., 1941. "Capillary Behavior in Porous Solids", Petroleum Technology, No. 1223, 152-169.

Macario, M. E., 1991, "Optimizing Reinjection Strategy in Palinpinon, Philippines Based on Chloride Data", M.S. Thesis, Stanford University, Stanford, CA.

Pamatian, P.I., 1997, "Changes in the Apparent Piezometric Levels in the Palinpinon Field as a Response to Twelve Years of Exploitation", Proceedings of 18th PNOC-EDC Geothermal Conference.

Pratt, W.K.: "Digital Image Processing", 1991, JohnWiley & Sons, Inc.

Pruess K. and Narasimhan T.N., 1985. "A Practical Method for Modeling Fluid and Heat Flow in Fracture Porous Media, SPE Journal, Vol. 25, No. 1, 14-26.

Pruess K., 1987. TOUGH User's Guide, Lawrence Berkeley National Laboratory, Berkeley, Calif.

Pruess K., 1991. TOUGH2-A General Purpose Numerical Simulator for Multiphase Fluid and Heat Flow, Report LBL-29400, Lawrence Berkeley National Laboratory, Berkeley, Calif.

Satik C. (1997a), Stanford Geothermal Program Quarterly Report June-September 1997, Stanford University.

Satik C. (1997b), "A Study of Boiling in Porous Media", Proc. 19th New Zealand Geothermal Workshop, Auckland, NZ.

Satik C. (1998), "A Measurement of Steam-Water Relative Permeability", Proc. of 23rd Workshop on Geothermal Reservoir Engineering, Stanford, Calif.

Sorey M.L., Grant M.A. and Bradford E., 1980. Nonlinear Effects in Two Phase Flow to Wells in Geothermal Reservoirs. Water Resources Research, Vol. 16 No. 4, pp 767-777.

Udell K. (1982). The thermodynamics of evaporation and condensation in porous media. SPE Paper 10779. Presented at SPE California Regional Meeting, San Francisco, CA, March 24-26, 1982.

van Genuchten M., 1980. “A Closed-Form Equation for Predicting the Hydraulic Conductivity of Unsaturated Soils”, Soil Sci. Soc. Am. J, 44(5), 892-898.